

Phase diagram of oxygen adsorbed on Ni(111) and thermodynamic properties from first-principles

C. Lazo*

Institute of Applied Physics and Microstructure Research Center, University of Hamburg, Jungiusstrasse 11, 20355 Hamburg, Germany

F. J. Keil

Institute of Chemical Reaction Engineering, Hamburg University of Technology, Eissendorfer Str. 38, 21073 Hamburg, Germany

(Received 13 November 2008; revised manuscript received 6 May 2009; published 12 June 2009)

The thermodynamic properties and the surface phase diagram of O/Ni(111) have been calculated from Metropolis and Wang-Landau Monte Carlo simulations based on lateral interactions derived from density-functional theory (DFT) calculations. The DFT energies were mapped onto an Ising-like Hamiltonian according to the cluster expansion technique formalism. Both fcc and hcp adsorption sites were included in the Hamiltonian. Different criteria were used to evaluate competing parameter sets: cross-validation score CV, Mallows's C_p statistics, and adjusted R^2 statistics. The parameter space was searched using genetic algorithms in order to find optimum parameter sets. The different parameter sets obtained from different criteria lead essentially to the same transition temperatures. Excellent agreement is found when comparing the shape and the stability regions of the theoretical and the experimental (from the literature) phase diagrams. We investigate the nature of the $p(2 \times 2)$ and $(\sqrt{3} \times \sqrt{3})R30^\circ$ phase transitions at $\Theta = 1/4$ and $1/3$ ML, respectively. Differences arise when comparing the values of the calculated and the experimental transition temperatures owing to imprecision in present-day DFT calculations.

DOI: [10.1103/PhysRevB.79.245418](https://doi.org/10.1103/PhysRevB.79.245418)

PACS number(s): 64.60.Cn, 68.43.De, 68.43.Fg, 02.70.Uu

I. INTRODUCTION

The collective behavior of atoms and molecules chemisorbed on a single-crystal substrate is characterized by their tendency to form distinct phases which possess well-defined two-dimensional periodicity and order. This phenomenon is caused by interactions between the adsorbed particles. The stability of a surface phase depends on the temperature T , the coverage Θ of the chemisorbed species, and intermolecular interactions. Phase transitions may occur depending on variations in (Θ, T) . The different adsorbate phases in (Θ, T) space for a particular system are conveniently described by means of the phase diagram of the system. The phase diagram of atoms and molecules adsorbed on surfaces is a central topic in surface science and is of great importance in describing the thermodynamics and kinetics of processes on surfaces such as adsorption, desorption, and catalytic reactions.

Much research has been carried out on phase transition at surfaces.¹⁻⁴ Experimentally, order-disorder phase transitions of chemisorbed species at surfaces can be quantitatively characterized by means of low-energy electron-diffraction (LEED) (Refs. 5 and 6) and scanning tunneling microscopy measurements.^{7,8}

The symmetry of ordered structures on surfaces is determined by the lateral interactions between the adsorbates. Therefore, the evaluation of sufficiently accurate lateral interaction parameters is essential for understanding phase transitions and other thermodynamic properties of adsorbed molecules or atoms on surfaces.

The development of computer power and first-principles methods, such as density-functional theory (DFT),⁹⁻¹¹ has enabled the derivation of interaction parameters with predictive power. Using such a technique, the phase diagrams of

O/Ru(0001) (Ref. 12) and O/Pt(111) (Ref. 13) have been studied, among others. Those systems, involving O and a metal surface, are the basis for a number of important technological processes such as bulk oxidation, corrosion, and heterogeneous catalysis. Thus, their understanding from macroscopic and microscopic points of view is of enormous importance.

The phase diagram of O/Ru(0001) from first-principles was based on a very small set of DFT calculations.^{12,14} Even though the shape of the calculated phase diagram agrees very well with the experimental one,¹⁵ the calculated transition temperatures are around 200 K higher than the experimental data. The phase diagram of O/Pt(111) from first-principles was based on a larger set of DFT calculations^{13,16} than in the case of O/Ru(0001). In particular, the authors carried out a ground-state search that considerably improved the precision of the derived interaction parameters. The O/Pt(111) phase diagram has not been experimentally determined; thus, a validation of the calculations was not yet possible.

The O/Ni(111) system has been extensively studied in the past, including studies of the phase diagram,^{17,18} lateral interactions,¹⁹ geometry of various phases,^{20,21} and critical properties.²²⁻²⁴ However, up to now, no theoretical calculations of the phase diagram based on first-principles have been carried out on this system. In this study, we pursue this aim and systematically compare our theoretical results with the experimental data in the literature.

The phase diagram of oxygen on Ni(111) has been studied from LEED experiments^{17,18} for the coverage range $0.1 \leq \Theta \leq 0.34$ ML and temperatures of 150–500 K (Fig. 1). At low temperatures a coexistence of lattice gas and of $p(2 \times 2)$ islands at coverages below 0.25 ML exists, which ends at the high-coverage side at the phase boundary to a homogeneous long-range-ordered $p(2 \times 2)$ phase that is

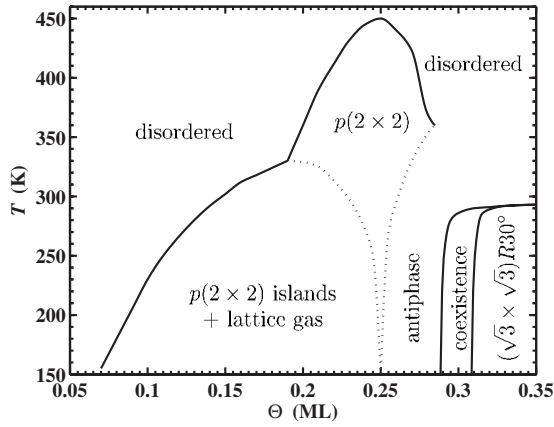


FIG. 1. Experimental phase diagram of the system O/Ni(111). Phase boundaries are marked by solid lines as far as measured, whereas dotted lines indicate necessary continuations, which are not quantitative (taken from Ref. 18).

stable at coverages close to 0.25 monolayer (ML) ($T_c \approx 440$ K). In the range $0.25 < \Theta < 0.29$ ML, splitting and streaking of the $p(2 \times 2)$ pattern is observed and interpreted to be due to the formation of antiphase $p(2 \times 2)$ domains. At even higher coverage of about 0.33 ML a well-ordered $(\sqrt{3} \times \sqrt{3})R30^\circ$ structure has been found in the experiments ($T_c \approx 300$ K). Also, a small coexistence region of $(\sqrt{3} \times \sqrt{3})R30^\circ$ and the antiphase structure is present.

Only fcc sites are occupied in the well-ordered $p(2 \times 2)$ and $(\sqrt{3} \times \sqrt{3})R30^\circ$ structures at low temperatures.^{20,21} However, the occupation of hcp sites can be activated at temperatures close to and above the order-disorder phase transitions.²⁵ At a temperature of above 500 K, Auger scans indicate that oxygen dissolves into the bulk and the dissolution process seems to be independent of coverage.^{17,24} At higher oxygen exposures ($\Theta > 0.4$ ML), oxide islands form which finally grow laterally to coalescence at about two to three layers of NiO.²⁶

To calculate the O/Ni(111) phase diagram theoretically, we derive lateral interaction parameters from DFT calculations using techniques from statistical mechanics, i.e., the cluster expansion (CE) method.^{27–31} The statistical-mechanics problem is numerically solved using Monte Carlo simulations based on the Metropolis³² and Wang-Landau^{33,34} algorithms. From those simulations, we are able to calculate (based only on computed energies from DFT calculations) the thermodynamic properties and the phase diagram of O/Ni(111). In the process, we gain deep insight into the lateral interactions producing the rich phase behavior shown by this system.

The outline of this paper is the following. Section II briefly describes the theoretical framework behind the first-principles statistical-mechanics approach used to calculate the O/Ni(111) phase diagram. Then, Sec. III summarizes the technical details of our DFT and Monte Carlo calculations, as well as the different criteria used to derive the O/Ni(111) lateral interaction parameters. Next, Sec. IV presents and discusses the results and compares them with previous experimental and theoretical studies in the literature. Finally, in Sec. V, we summarize the results of this study.

II. THEORY

The theoretical description of phase transitions is based on the equations given by equilibrium thermodynamics. All systems in thermodynamic equilibrium are at a minimum of their free energy,

$$F = U - TS. \quad (1)$$

Phases highly ordered at microscopic level are typically present at low temperatures T , where the energy U is the dominant quantity in Eq. (1), i.e., the phases present at low temperatures are the ones exhibiting low energy (ground states). As the temperature increases, the entropic term in Eq. (1) becomes more important and phases with a high entropy, i.e., high degree of disorder at the microscopic level, are present.

The link between the microscopic properties of matter and its macroscopic properties is provided by the concepts of statistical mechanics.³⁵ Within the statistical-mechanics formalism, the free energy $F(T)$ is given by³⁵

$$F = -k_B T \ln Z, \quad (2)$$

where k_B is the Boltzmann constant and Z is the partition function of the system given by

$$Z = \sum_i e^{-E_i/k_B T}. \quad (3)$$

The sum in Eq. (3) runs through all available microstates i of the system.

One can *numerically* derive thermodynamic quantities from Z by means of Monte Carlo methods. Those methods considerably reduce the calculations needed. However, one still needs a sizable number of energy evaluations ($>10^6$) in order to calculate thermodynamic properties. Besides, the size of the system under study has to be large enough so as to ensure that its thermodynamic properties correspond or are close to the thermodynamic limit, i.e., to the properties of an infinite system. Those requirements (many energy evaluations and a proper system size) impede the execution of Monte Carlo simulations where all required energies are directly evaluated from (expensive) DFT calculations. Thus, in order to be able to carry out Monte Carlo simulations employing energies from DFT calculations, one needs to map DFT results onto a simpler model of the system.

For chemisorbed adsorbates, the wells of the surface potential are steep and deep. The locations of the minima of the so-called corrugation potential thus form a well-defined lattice, at which the occupation probability density of adsorbates is sharply peaked. Then, in the study of equilibrium properties of adsorbed overlayers, one can neglect deviations of the adsorbate positions from the sites of this “preferred lattice” altogether and can introduce the lattice-gas model for the study of adsorbates on surfaces.

In the lattice-gas model the complex many-body interactions in the adsorbate/substrate system are approximated to lateral interactions among the adsorbates on the surface. The energy of the system is then given by an Ising-like Hamiltonian³⁶

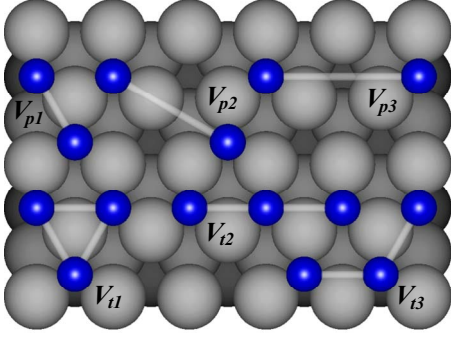


FIG. 2. (Color online) Lateral interactions between and among atoms adsorbed on the fcc sites of a (111) surface. p and t denote pair and trio interactions, respectively.

$$\mathcal{H}(n) = \sum_i V_i n_i + \sum_{i,j} V_{ij} n_i n_j + \sum_{i,j,k} V_{i,j,k} n_i n_j n_k + \dots \quad (4)$$

Here, V_i is the energy of an isolated atom; $V_{ij} = V_{p1}, V_{p2}, V_{p3}, \dots$ is the pair interaction energy of nearest, next-nearest, third-nearest neighbors, and so on, respectively; and V_{ijk} is the energy of trio interactions (see Fig. 2); higher-order terms (quartets, quintets, etc.) can also be included into the expansion.

In order to specify a configuration, a site occupation variable is assigned to each adsorption site on the surface. Different choices for the site occupation variables are possible. In this study we use the so-called ‘‘point variables’’ $n_i = 1$ (occupied) and 0 (vacant). However, due to their correspondence with the Ising model, ‘‘spin variables’’ are also possible, $\sigma_i = +1$ (occupied) and -1 (vacant). The relation between n_i and σ_i is given by $n_i = 0.5(1 + \sigma_i)$. Our choice of using point variables, i.e., n_i , is due to the fact that they lead to lateral interactions V between oxygen atoms on the surface that have physical meaning.^{37,38} Besides, when considering trio interactions, seemingly modest spin interactions J 's can correspond to enormous unphysical lattice-gas energies V 's. The reason for that is the highly nonlinear relation between spin and lattice-gas interactions.^{37,38}

The sum in Eq. (4) runs over all the ‘‘cluster figures’’ included in the expansion (a cluster is defined by a set of lattice points). In other words, the sums in Eq. (4) count the frequency that a determined cluster figure appears in a specific configuration.

By calculating the lateral interactions among the adsorbates on the surface, the lattice-gas model accounts for the relevant quantities responsible for the collective behavior of atoms on surfaces. However, one has to bear in mind that the lateral interactions of the lattice-gas model are effective representations of the complex many-body interactions in the adsorbate/substrate system.

It can be shown³⁹ that when all lateral interactions are taken into account in the sum, Eq. (4), the expansion is able to represent any function $E(n)$ of configuration n by an appropriate choice of V values. The formalism of expanding the energy (or other quantity) as a function of the lateral interactions (or cluster figures) is known as the CE method,^{27,30,31} and the lateral interaction parameters V are

known as effective cluster interactions (ECIs).

Even though the accuracy of the CE is strictly valid at the infinite limit, practically one cannot consider all the terms in the sum, and the expansion has to be truncated. In general, one could expect that the expansion would converge rapidly after keeping only cluster figures that are relatively compact (e.g., short-range pairs or small triplets). There is, however, no formal proof of the latter assumption, and the accuracy of the truncated expansion should be checked. The big advantage of the CE is its ability to rapidly calculate the energy $E(n)$ for any arbitrary configuration. This ability renders the technique useful for sampling the configuration space in Monte Carlo simulations.

The unknown parameters of the cluster expansion, V_i , are determined by fitting them to the energy of a relatively small number of configurations obtained through first-principles DFT computations (this approach is known as the structure inversion method or the Connolly-Williams method⁴⁰). For this purpose, one has to solve a linear system of equations,

$$\mathbf{E} = \mathbf{\Sigma} \mathbf{V}, \quad (5)$$

where \mathbf{E} is the vector of calculated DFT energies for a set of different adsorbate configurations, \mathbf{V} is the vector of the unknown ECI energies, and $\mathbf{\Sigma}$ is the matrix of occupation variables n_i for every ECI of every included adsorbate configuration.

Once the ECIs have been derived, the Hamiltonian in Eq. (4) was used to perform Monte Carlo simulations, i.e., temperature effects have been introduced into the system. In this way, Monte Carlo calculations with first-principles accuracy were carried out.

III. COMPUTATIONAL METHODS

A. Energies from first-principles calculations

One of the most important outputs of the first-principles calculations is the total energy of the system. However, in order to compare different structures with each other on the same basis, one often calculates the gain in energy of the adsorbate/substrate system with respect to the free substrate (clean surface) and the free molecule, i.e., the average change in energy per atom due to adsorption (or simply called here E_a). For the case of the O/Ni(111) system, E_a per atom at coverage Θ is given by

$$E_a^\Theta = \frac{1}{N_O} \left(E_{\text{O/Ni(111)}}^\Theta - E_{\text{Ni(111)}} - \frac{N_O}{2} E_{\text{O}_2} \right), \quad (6)$$

where $E_{\text{O/Ni(111)}}^\Theta$ is the total energy of the slab containing the oxygen adsorbate at a coverage Θ , $E_{\text{Ni(111)}}$ is the total energy of the corresponding clean Ni(111) slab, E_{O_2} is the total energy of an isolated oxygen molecule, and N_O is the total number of O atoms present in the unit cell at the considered coverage Θ . The definition is such that a negative value of E_a^Θ indicates that the dissociative adsorption of the molecule is exothermic at $T=0$ K.

From E_a data one can readily derive lateral interaction parameters. However, for purposes of understanding phase stability, it is often convenient to consider formation energies

instead of E_a energies. The formation energy of a particular configuration at a given coverage, Θ , of oxygen on Ni(111) is given by

$$\Delta E_f^\Theta = \frac{1}{N} [E_{\text{O/Ni(111)}}^\Theta - (1 - \Theta)E_{\text{Ni(111)}} - \Theta E_{p(1 \times 1)\text{-O}}], \quad (7)$$

where $E_{\text{O/Ni(111)}}^\Theta$ and $E_{\text{Ni(111)}}$ have the same meaning as before, $E_{p(1 \times 1)\text{-O}}$ is the total energy of oxygen adsorbed on Ni(111) at full coverage, and N is the total number of adsorption sites. The formation energy reflects the relative stability of a particular configuration with respect to phase separation into a fraction Θ with full coverage $p(1 \times 1)$ and a fraction $(1 - \Theta)$ of empty sites (clean surface) at the same overall composition.

The formation energy allows for determining the ground-state structures by constructing the convex hull connecting the lowest-energy points in the $(\Delta E_f, \Theta)$ plot.^{27,41} Thus, formation energies are the central quantities in order to study O/Ni(111) phase stability. The change in energy due to adsorption and the formation energy at Θ are simply related by

$$\Delta E_f^\Theta = \Theta(E_a^\Theta - E_a^{1 \text{ ML}}), \quad (8)$$

where E_a^Θ is given by Eq. (6) and $E_a^{1 \text{ ML}}$ is E_a of oxygen adsorbed on Ni(111) at full coverage.

The use of formation energies is very convenient for determining the convergence parameters of the DFT basis set. The size of the basis set that leads to converged formation energies, i.e., E_a differences [Eq. (8)], is significantly smaller than the one needed for converged E_a energies. It is the difference in E_a energies (and not their absolute values) that are the quantities that determine the transition temperatures. These differences are conveniently expressed by formation energies [Eq. (8)]. Thus, we determined the parameters of the DFT basis set from formation energy convergence tests. Afterward, with this basis set, we calculated E_a energies to derive the lateral interactions V of Eq. (4). In adsorption of atoms on surfaces, the physical discussion of interactions derived from E_a energies is simpler and more intuitive than the discussion of interactions derived from formation energies.

B. DFT basis set and convergence

First-principles DFT was used to compute the total energies. The DFT total energies were obtained using the full-potential augmented plane wave + local orbitals (APW+lo) and the linear augmented plane-wave (LAPW) method as implemented in the WIEN2K^{42,43} code. Exchange and correlation effects were included in the generalized gradient approximation (GGA) using the functional of Perdew, Burke, and Ernzerhof (PBE).⁴⁴ Since O/Ni(111) is a magnetic system, the DFT results reported below are from spin-polarized calculations.

The Ni(111) surface is modeled using supercell geometries containing fully relaxed symmetric slabs with five layers and 15 Å vacuum between subsequent slabs. Oxygen atoms are adsorbed on both sides of the slab. We have also performed test calculations with thicker slabs and more vacuum, without obtaining any significant differences with

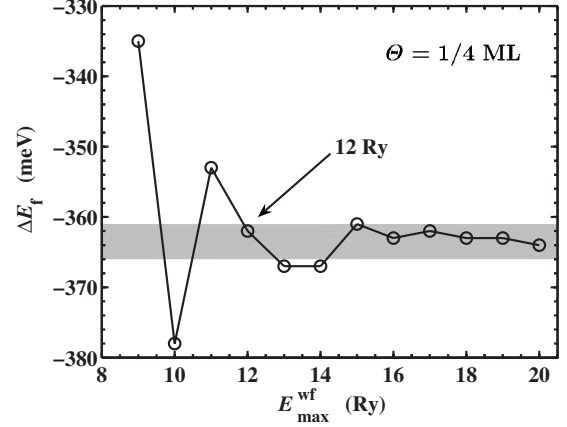


FIG. 3. Formation energy ΔE_f versus energy cutoff $E_{\text{max}}^{\text{wf}}$ for $\Theta = 1/4$ ML. The convergence range is 5 meV wide and is indicated by the gray area. The convergence threshold ($E_{\text{max}}^{\text{wf}} = 12$ Ry) is indicated by the arrow.

respect to the chosen setup (see the Appendix).

If it is not indicated otherwise, the parameters of the mixed APW+lo and the LAPW basis set are $R_{\text{MT}}^{\text{Ni}} = 2.0$ bohr, $R_{\text{MT}}^{\text{O}} = 1.4$ bohr (the nonoverlapping muffin-tin spheres were chosen as large as possible to keep the required interstitial plane-wave cutoff as low as possible), wave-function expansion inside the muffin tins up to $l_{\text{max}}^{\text{wf}} = 12$, and potential expansion up to $l_{\text{max}}^{\text{wf}} = 6$. A $(12 \times 12 \times 1)$ Monkhorst-Pack grid was used for the (1×1) Brillouin-zone integration. The integration grid includes the Γ point. For the other surface unit cells used in the calculations, grids have been chosen so as to obtain the same sampling of the reciprocal space. This ensures compatible results from calculations carried out in different surface unit cells.

A temperature broadening with a Fermi function⁴⁵ is used with a broadening parameter $T^{\text{el}} = 0.005$ Ry in order to reduce the number of \mathbf{k} points that are necessary to calculate the total energy of the metallic system. The total energy is corrected corresponding to $T = 0$ K. Core states are treated fully relativistically and, for the valence states, relativistic effects are included in a scalar relativistic treatment.

The energy cutoff for the plane-wave representation in the interstitial region is $E_{\text{max}}^{\text{wf}} = 12$ Ry for the wave function and $E_{\text{max}}^{\text{pot}} = 196$ Ry for the potential. $E_{\text{max}}^{\text{wf}}$ is the most critical parameter affecting the accuracy of the calculations and convergence tests are necessary to determine it. Figure 3 shows a convergence test carried out to determine $E_{\text{max}}^{\text{wf}}$. The converged quantity is the formation energy at $\Theta = 1/4$ ML. The calculations were carried out in a (2×2) surface unit cell. The convergence range is 5 meV wide and is indicated by the gray area. The energy cutoff used in the first-principles calculations for the O/Ni(111) system was determined from the convergence threshold in Fig. 3 and is indicated by an arrow.

As is evident from Fig. 3, formation energies are converged within 5 meV regarding $E_{\text{max}}^{\text{wf}}$. Similar tests regarding the \mathbf{k} -mesh grid lead to convergence within 1–2 meV. Thus, the numerical uncertainty of the basis set parameters used for the O/Ni(111) system is very low and, as will become apparent below, does not affect our discussion and conclusions.

C. Derivation of lateral interaction parameters

It has been shown that the lateral interaction parameters (or effective cluster interactions in the CE language) can be interpreted as lattice averages of interatomic potentials.⁴⁶ Even though they have a well-defined physical meaning, their value can only be obtained as a statistical average. Thus, when dealing with the linear system of equations described at the end of Sec. II, one should compute more DFT energies E than the ECIs V being considered [see Eq. (5)]. In this way, one optimizes the value of the ECIs by reducing the error (least-squares method) between the DFT energies and the corresponding energy value given by the Hamiltonian in Eq. (4).

Thus, the problem of extracting lateral interactions from first-principles calculations can be formulated as a regression problem, i.e., one can apply the statistical methods used to investigate the relationship between a dependent or response variable y and one or more independent variables x . The independent variables (in this case, V) are usually called regressor variables or predictor variables (see, e.g., Ref. 47).

The problem, then, consists of selecting an appropriate set of lateral interactions (regressors) from a set that quite likely includes all the important variables.⁴⁸ In such a situation, one is interested in *variable selection*, that is, screening the candidate variables to obtain a regression model that contains the “best” subset of regression variables with respect to the intended use of the model (e.g., prediction). An effective approach to search the parameter space for the best model is based on genetic algorithms,^{49,50} and we shall use this approach to screen the parameter space of the O/Ni(111) Hamiltonian.

Several criteria may be used to evaluate competing regression models. A commonly used criterion is based on minimizing the cross-validation score (CV),^{28,51} which is defined as the average of the sum of the squares of the differences between each observation y_i and the corresponding predicted value based on a least-squares fit to the *remaining* $n-1$ points, say $\hat{y}_{(i)}$. Thus, CV provides a measure of how well the model is likely to perform when predicting *new* data or data that were not used to fit the regression model. The computing formula for CV is

$$(\text{CV})^2 = \frac{1}{n} \sum_{i=1}^n (y_i - \hat{y}_{(i)})^2. \quad (9)$$

The optimal subset of regression variables found using the CV score frequently includes long-range or multisite cluster figures without including shorter ones.⁵⁰ This is an undesirable feature since cluster expansions constructed in that way imply that the ECI are void of any physical meaning and are treated as stochastic variables only.⁵² Thus, other statistical criteria that directly assess the explanatory effect of every individual cluster figure might be helpful in evaluating competing regression models.

Mallow's C_p statistics⁴⁷ is a direct function of the residual sum of squares that incorporates a penalty for each variable added to the model to protect against overfitting. The computing formula for Mallow's C_p statistics is

$$C_p = \frac{\text{SS}_E(p)}{\hat{\sigma}^2} - n + 2p, \quad (10)$$

where n is the number of observations, p is the number of parameters in the reduced model, $\text{SS}_E(p)$ is the residual sum of squares for the reduced model with p parameters, and $\hat{\sigma}^2$ is the estimate of the mean square error of the full model. The regression equations that have negligible bias will have values of C_p that are close to p , while those with significant bias will have values of C_p that are significantly greater than p . One then chooses as the best regression equation either a model with *minimum* C_p or a model with a slightly larger C_p that does not contain as much bias (i.e., $C_p \cong p$). The interpretation of the C_p approach is given by Gilmour.⁵³

Another common criterion for evaluating and comparing the different regression models obtained is the adjusted R^2 statistics,⁴⁷

$$R_{\text{adj}}^2 = 1 - \frac{\text{SS}_E/(n-p)}{\text{SS}_T/(n-1)}, \quad (11)$$

where n is the number of observations, p is the number of unknown regressors, SS_E is the residual sum of squares, and SS_T is the total sum of squares. R_{adj}^2 is just a correlation coefficient adjusted for the degrees of freedom. Because $\text{SS}_E/(n-p)$ is the error or residual mean square and $\text{SS}_T/(n-1)$ is a constant, R_{adj}^2 will only increase when a variable is added to the model if the new variable reduces the error mean square. The R_{adj}^2 statistics essentially penalizes for adding terms to the model. It is an easy way to guard against overfitting, i.e., including regressors that are not really useful. Consequently, it is very useful in comparing and evaluating competing regression models. Usually, the model that *maximizes* R_{adj}^2 , i.e., $R_{\text{adj}}^2 \leq 1$, is considered to be a good candidate for the best regression equation.

No single algorithm will always produce an optimum solution to the variable selection problem. In practice, the alternatives can lead to different model choices. We shall consider the three criteria listed above, coupled with a genetic-algorithm searching strategy, in order to find optimal models. We shall also assess how our results depend on the chosen criteria. Note that it is possible that none of the fits can be considered the best one, i.e., all or some of them could lead to acceptable results.

D. Monte Carlo simulations

The thermodynamics of the O/Ni(111) lattice-gas model are calculated numerically by Metropolis Monte Carlo simulations.^{32,54} The simulations were performed in the canonical (temperature T and coverage Θ constant) and grand canonical (temperature T and chemical potential μ constant) ensembles, using Kawasaki and Glauber samplings,⁵⁴ respectively.

To measure continuous order-disorder phase transitions in canonical Monte Carlo simulations, order parameters are defined according to the symmetry broken during the transition. We use two order parameters ψ and ϕ as defined in Refs. 55 and 56, which are nonzero for the $p(2 \times 2)$ and $(\sqrt{3} \times \sqrt{3})R30^\circ$ phases, respectively.

To measure the $p(2 \times 2)$ phase, the triangular lattice formed by the fcc sites of the Ni(111) surface is decomposed into four triangular $p(2 \times 2)$ sublattices. Defining the population on the p th (2×2) sublattice by N_p ($p=1, 2, 3, 4$), the order parameter is

$$\psi = \frac{1}{\sqrt{3}N}(\psi_1^2 + \psi_2^2 + \psi_3^2), \quad (12)$$

where

$$\psi_1 = N_1 + N_2 - N_3 - N_4,$$

$$\psi_2 = N_1 - N_2 + N_3 - N_4,$$

$$\psi_3 = N_1 - N_2 - N_3 + N_4,$$

and $N=N_1+N_2+N_3+N_4$ is the total number of adsorbed atoms present.

To measure the $(\sqrt{3} \times \sqrt{3})R30^\circ$ phase, the triangular lattice formed by the fcc sites of the Ni(111) surface is decomposed into three sublattices made up of sites connected by next-nearest-neighbor bonds. Defining the population of the p th $(\sqrt{3} \times \sqrt{3})R30^\circ$ sublattice by N_p ($p=1, 2, 3$), the order parameter is

$$\phi = \sqrt{\phi_1^2 + \phi_2^2}, \quad (13)$$

where

$$\phi_1 = \frac{3}{2N} \left(N_1 - \frac{1}{2}(N_2 + N_3) \right),$$

$$\phi_2 = \frac{3\sqrt{3}}{4N} (N_2 - N_3),$$

and, as before, $N=N_1+N_2+N_3$ is the total number of adsorbed atoms present.

The order parameters given by Eqs. (12) and (13) do not converge precisely to zero as the order to disorder transition is crossed due to the finite size of the system. The transition temperature T_c at a given coverage is given by the inflection point in the calculated graph of order parameter versus temperature. For that purpose, one performs scans on the system at constant Θ varying T (alternatively, the order-disorder T_c can also be determined by finding the temperature at which the heat capacity of the system peaks⁵⁴).

In case of first-order transitions, simulations in the canonical ensemble can lead to wrong results due to finite size effects and phase coexistence. The thermodynamic properties of the system are affected by non-negligible energy contributions from the boundaries of every coexisting phase.^{6,54} In order to avoid this problem, one lets the system to exchange energy and particles with a reservoir, i.e., one carries out simulations in the grand canonical ensemble.

Thus, in order to locate first-order phase transitions, we carried out simulations in the grand canonical ensemble and performed scans at constant T varying μ . For that purpose, the only modification needed in the Hamiltonian \mathcal{H} of Eq. (4) is to subtract the term $\mu \sum_i n_i$ from the right-hand side of the equation.⁶

From the chemical-potential versus number of atoms data (μ, N) obtained from the simulations, the grand canonical potential Φ_G is calculated by integrating the thermodynamic relation

$$\left(\frac{\partial \Phi_G}{\partial \mu} \right)_{V,T} = -N. \quad (14)$$

The integration was performed numerically by fitting cubic splines to the data points.

The integration of Eq. (14) was carried out *separately* for the two phases participating in the transition (in order to avoid inaccuracies of the simulation data at the phase transition). The interception of the two grand potential curves (in a Φ_G versus μ plot) determines the location of the chemical potential of the transition (μ^*). The coverage of every phase present at the phase-coexistence region can then be obtained by determining the two values of $\langle N \rangle$ (in the hysteresis loops of the transition) corresponding to μ^* .

Suitable reference states⁵⁷ have to be used in order to integrate Eq. (14) for every coexisting phase. To obtain Φ'_G at the constant temperature of integration T' in Eq. (14), we integrated T versus U data from canonical Monte Carlo simulations in order to obtain the entropy S from the relationship

$$T \left(\frac{\partial S}{\partial T} \right)_{V,N} = \left(\frac{\partial U}{\partial T} \right)_{V,N} \quad (15)$$

[the reference state of the entropy for the integration of Eq. (15) can be conveniently taken as zero for nondegenerate ground states at $T=0$ K].⁵⁴ Once $S(T')$ is known, the Helmholtz free energy $F(T')$ is calculated from Eq. (1) and the initial grand potential for the integration of Eq. (14) is obtained from

$$\Phi'_G = F(T', V', N') - \mu' N'. \quad (16)$$

Thus, Eqs. (14) and (15) were integrated along horizontal and vertical paths, respectively, in (Θ, T) space, in order to locate first-order transitions.

The Metropolis Monte Carlo simulations were carried out on a honeycomb (60×60) two-dimensional lattice with periodic boundary conditions. This lattice allows the inclusion of fcc and hcp sites. The shape of the unit cell was a rhombus. Convergence studies of the phase diagram with respect to increased lattice sizes lead essentially to the same transition temperatures. Two thousand Monte Carlo steps per site are used for equilibration, followed by 10 000 Monte Carlo steps for sampling at each (T, Θ) and (T, μ) sampling point (one Monte Carlo step correspond to randomly picking N sites and thus generating N trial states; where N denotes the total number of sites in the lattice).

Additionally, we carried out Wang-Landau^{33,34} Monte Carlo simulations in the canonical ensemble to study the nature of the phase transitions at $\Theta=1/4$ and $1/3$ ML. By shifting the acceptance rule from energy to entropy space, the Wang-Landau algorithm is able to surmount the problem posed by hysteresis at first-order phase transitions and critical slowing down at continuous phase transitions. From Wang-Landau Monte Carlo simulations, one obtains the con-

TABLE I. Structural, magnetic, and energetic properties of bulk Ni and the Ni(111) surface. Lattice constant a , bulk magnetic moment M_B , top layer relaxation as percent change with respect to the bulk value Δ_{12} , work function Φ , magnetic moment in the surface M_S , and surface energy σ . FP denotes the full-potential DFT-GGA results of this work and PP denotes the pseudopotential DFT-GGA results of Ref. 58.

	a (Å)	M_B (μ_B)	Δ_{12} (%)	Φ (eV)	M_S (μ_B)	σ (eV/atom)
FP	3.54	0.63	-1.6	5.12	0.75	0.66
PP ^a	3.53	0.61	-0.9	5.11	0.68	0.65
Expt. ^b	3.52	0.61	<2.0	5.35		0.82

^aReference 58.

^bReferences 59–62.

figural density of states, $\Omega(E)$ and with it all thermodynamic information about the system (see Ref. 34 for details).

The Wang-Landau Monte Carlo simulations are carried out on a honeycomb (60×60) two-dimensional lattice with periodic boundary conditions. To calculate $\Omega(E)$, the energy is discretized into 7000 equal size intervals (i.e., of the same order of magnitude as the total number of sites³⁴). Parallel runs are performed for different energy ranges and the resulting parts of the configurational density of states are pieced together in order to obtain the total $\Omega(E)$.³⁴ Further parameters in the algorithm (initial and final modification factors, modification factor reduction schedule, and histogram flatness criterion) are selected according to the standard specifications of the algorithm.³⁴

IV. RESULTS

A. DFT calculations

The results of the calculations for the bulk Ni and the clean Ni(111) surface are presented in Table I. The bulk lattice constant a and the bulk magnetic moment M_B are in excellent agreement with pseudopotential (PP) DFT-GGA calculations from the literature and experimental results.^{58–62} The Ni(111) clean surface exhibits only a marginal inward relaxation of -1.6% in the first layer with respect to the Ni bulk interlayer spacing. The work function Φ and the surface energy σ match the PP values but they noticeably deviate from experiments by 4.3% and 19.5%, respectively.

Adsorbed atomic oxygen on Ni(111) was calculated on several high-symmetry sites (see Fig. 4) for a $p(2 \times 2)$ superstructure. For this set of calculations it was necessary to reduce the muffin-tin radius of oxygen to 1.1 bohr in order to calculate the energy of the O_2 molecule and to allow for O-Ni relaxations in all high-symmetry sites [the O-Ni distance of O at the top site is much shorter than O at the threefold hollow sites (see Table II)]. Since $R_{MT}^O = 1.1$ bohr is smaller compared to the value used for the convergence test illustrated in Fig. 3, the kinetic energy cutoff for the plane-wave basis needed for the interstitial region is larger ($E_{max}^{wf} = 25$ Ry, after a similar test as the one in Fig. 3, other parameters as in Sec. III B). The energy of the O_2

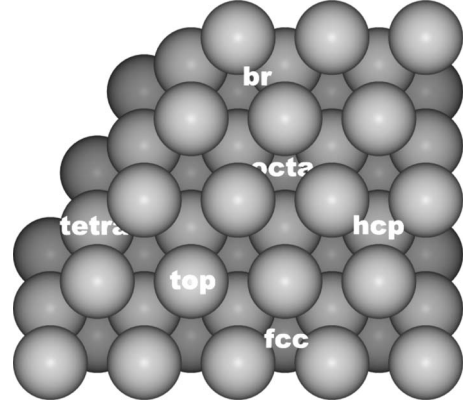


FIG. 4. High symmetric adsorption sites of the Ni(111) surface. fcc and hcp denote the threefold on-surface sites. Top denotes the on-top site above a surface atom and br is the bridge site between the fcc and hcp sites. Directly below the hcp site and above a metal atom in the second layer is the tetrahedral subsurface (tetra) site. Directly below the fcc site and above a metal atom in the third layer is the octahedral subsurface (octa) site.

molecule was calculated using a rectangular cell of dimension $15 \times 16 \times 17$ bohr³ with Γ -point sampling.

The subsurface configurations [octa and tetra (see Fig. 4)] were calculated using supercell geometries containing seven layers of Ni(111). Correspondingly, the fcc $p(2 \times 2)$ superstructure was additionally calculated using seven layers of Ni(111) to obtain the energy differences of the subsurface sites reported in Table II.

For the fcc site, we obtained $E_a = -2.88$ eV, which significantly differs from the calorimetry experimental⁶⁵ value of -2.28 eV. This overbinding is in the range of current DFT functionals. For a discussion of this point, see, e.g., Refs. 66–68. In case of strong dispersive interactions, often a too

TABLE II. Calculated properties of O at the high-symmetry sites of Ni(111) (see Fig. 4) for $\Theta = 1/4$ ML in a (2×2) surface unit cell. ΔE_a is the E_a difference with respect to the E_a of the fcc site (-2.88 eV from our calculations), d_{Ni-O} is the distance to the nearest Ni atom (for the subsurface positions also the distance to the nearest Ni atom in the subsurface layer is given in parentheses), and Δ_{12} is the top layer relaxation as percentage change with respect to the bulk value (the center of mass of the Ni top layer is used in this definition).

Sites	ΔE_a (eV)	d_{Ni-O} (Å)	Δ_{12} (%)	ΔE_a^a (eV)	ΔE_a^b (eV)
fcc	0.00	1.85	0.0	0.00	0.00
hcp	0.13	1.84	0.5	0.12	0.08
br	0.61	1.80	-0.1	0.55	0.82
top	2.06	1.69	-1.8	1.84	1.86
octa	2.48	1.86(1.97)	8.6		
tetra	2.58	1.76(1.81)	10.9		

^aResults taken from Eichler *et al.* using the PW91 exchange-correlation functional (Ref. 63).

^bResults taken from Li *et al.* using the PW91 exchange-correlation functional (Ref. 64).

TABLE III. Calculated and experimental (from the literature) structural parameters in Å for the $p(2 \times 2)$ and $(\sqrt{3} \times \sqrt{3})R30^\circ$ configurations of O in the fcc-hollow sites of Ni(111). For the interlayer distances d , the center of mass of each Ni layer is used. $d_{\text{Ni-O}}$ is the O-Ni bond length, Δz_1 is the buckling of the first layer, and Δx_1 is the adsorbate-induced lateral shift of the Ni atoms in the first layer.

Structure		$d_{\text{Ni-O}}$	d_{01}	d_{12}	Δz_1	Δx_1
$p(2 \times 2)$	DFT	1.85	1.15	2.02	0.09	0.01
	Expt. (Ref. 21)	1.83	1.11	2.05	0.09	0.02 ± 0.04
	Expt. (Ref. 73)	1.83 ± 0.03	1.10 ± 0.03	2.04 ± 0.03	0.12 ± 0.03	0.07 ± 0.03
	Expt. (Ref. 70)	1.85 ± 0.05		2.18 ± 0.10		
$(\sqrt{3} \times \sqrt{3})R30^\circ$	DFT	1.84	1.13	2.06	0	0
	Expt. (Ref. 20)	1.80 ± 0.02	1.08 ± 0.02	2.05 ± 0.02	0	0
	Expt. (Ref. 70)	1.85 ± 0.05		2.18 ± 0.10		

small E_a has been observed (e.g., Ref. 69). However, as is evident from the discussion regarding Eqs. (7) and (8), the quantities that govern the phase-transition behavior of adsorbates on surfaces are the *differences* in E_a energies and not their absolute values. Thus, the E_a energies reported in this study correspond to converged energy differences.

E_a differences, ΔE_a , of O adsorbed in the high-symmetry sites of the Ni(111) surface are reported in Table II. The fcc adsorption site is the most stable, in agreement with experimental findings.⁷⁰ The fcc site is only slightly more favorable than the hcp site (0.13 eV difference), while adsorption at bridge, top, and subsurface sites has less favorable E_a energies. This confirms the usual trend of oxygen to occupy high coordinated sites. The oxygen distance to the nearest Ni atom, $d_{\text{Ni-O}}$, and the top layer relaxation, Δ_{12} , are in very good agreement with previous DFT calculations.^{63,64}

There is some disagreement when comparing our on-surface E_a differences (full-potential LAPW/APW+lo) with the results from Eichler *et al.*⁶³ and Li *et al.*⁶⁴ based on pseudopotentials. Even though the trends are the same, the absolute value of the E_a differences varies from set to set. Similar unsatisfactory scattering of published DFT energy results has already been documented and systematically studied for the adsorption of O and CO at RuO₂(110).⁷¹ For that case, it was concluded that tiny imprecisions appearing in the scattering properties of f -like waves in the frozen-core approximation lead to significant differences with respect to results obtained from full-potential LAPW/APW+lo calculations.

In general, the replacement of core electrons by an effective core potential in a PP calculation is done to reduce computational cost and should, ideally, give results identical to those of an all-electron (AE) calculation using the same functional. However, the replacement of the full AE potential with a PP is a delicate undertaking that involves an inherent tension between optimal transferability (faithful reproduction of AE atom behavior) and improved computational efficiency (slowest possible spatial variability). Whenever possible, one should carry out comparison tests with AE calculations to ensure that the PP results are correct within the DFT level of approximation used.⁷² The quality of PP and AE calculations, properly executed, should be nearly the same.⁷¹

Based on the results presented in Table II, one would expect O to occupy mostly fcc and hcp sites on the Ni(111) surface at temperatures near the order-disorder phase transition. Thus, those are the adsorption sites that we will consider in our lattice-gas model for the O/Ni(111) system. The energy results in Table II indicate that adsorption on subsurface sites is clearly unfavorable with respect to adsorption on the threefold hollow sites. Consequently, we shall not include subsurface sites in the lattice model for O/Ni(111).

O on Ni(111) is known to be a magnetic system^{74,75} and, consequently, the DFT results in this study are the result of spin-polarized calculations. We have not carried out nonmagnetic calculations. However, previous calculations⁷⁵ for the $(\sqrt{3} \times \sqrt{3})R30^\circ$ structure have shown that different results are obtained for ΔE_a depending on the magnetization of the system. According to the results in Ref. 75, the difference in ΔE_a for the fcc and hcp sites for the nonmagnetic case is 0.34 eV, while for the magnetic case is 0.16 eV. As we will see below, the difference between both sets of results (0.18 eV) is of the same order of magnitude as the lateral interactions derived from DFT data. Thus, we expect that nonmagnetic calculations would lead to different interaction than magnetic ones.

The calculated and the experimental (from the literature) atomic geometry data for the $p(2 \times 2)$ and the $(\sqrt{3} \times \sqrt{3})R30^\circ$ structures of O in the fcc-hollow sites are summarized in Table III. Good agreement (within the experimental error bars) between the data is observed. In the $p(2 \times 2)$ structure, oxygen pushes its three Ni neighbors radially away ($\Delta x_1 = 0.01$ Å) and lifts them up. This is counteracted by a downward movement of the non-O-coordinated Ni atom, leading to a modest first layer buckling of $\Delta z_1 = 0.09$ Å. Lateral shifts and vertical buckling in the first Ni layer of the $(\sqrt{3} \times \sqrt{3})R30^\circ$ structure are excluded by symmetry.²⁰

Vibrational frequencies for the $p(2 \times 2)$ configuration of O on Ni are calculated by numerical differentiation of the forces using a second-order finite-difference approach with a step size of 0.02 Å. The Ni atoms are fixed in their relaxed geometries; only the oxygen atoms are explicitly moved. This approximation is not expected to introduce significant error into the results since the O and Ni vibrations modes are reasonably decoupled ($\bar{\nu}_{\text{max}}^{\text{Ni}} = 295$ cm⁻¹).⁷⁶ The Hessian ma-

TABLE IV. Symmetric stretching $\bar{\nu}_\perp$, asymmetric stretching $\bar{\nu}_{\parallel x}$, and asymmetric stretching $\bar{\nu}_{\parallel y}$ for 1/4 and 1/3 ML of O adsorbed on the fcc and hcp sites of Ni. The corresponding ZPEs are also given.

Θ (ML)	Sites	$\bar{\nu}_\perp$ (cm^{-1})	$\bar{\nu}_{\parallel x}$ (cm^{-1})	$\bar{\nu}_{\parallel y}$ (cm^{-1})	ZPE (meV)
1/4 ^a	fcc	550	456	449	90
	hcp	545	435	451	89
1/3 ^b	fcc	538	400	413	84
	hcp	524	410	424	84

^aCalculations using a (2×2) unit cell.

^bCalculations using a $(\sqrt{3} \times \sqrt{3})R30^\circ$ unit cell.

trix is mass weighted and diagonalized to yield the frequencies and the normal modes of the system. The results presented in Table IV are in reasonable agreement with experimentally measured⁷⁷ $p(2 \times 2)$ O/Ni(111) frequencies: 573, 540, and 452 cm^{-1} ; however, a definite assignment is not possible.

The zero-point energies (ZPE) are also reported in Table IV for both sites: fcc and hcp. The energies are almost the same for both sites. This is reasonable since, geometrically, the two adsorption sites (fcc and hcp) are very similar (see Fig. 4). As a consequence, the energy differences between the fcc and the hcp $p(2 \times 2)$ structures are not affected by their ZPEs.

Furthermore, Table IV shows the vibrational frequencies and the ZPE for the $(\sqrt{3} \times \sqrt{3})R30^\circ$ $\Theta=1/3$ ML configuration. The values are close to those for the $p(2 \times 2)$ configuration. The ZPEs differ by only ≈ 5 meV. Thus, within the harmonic approximation, the effects of the vibrational entropy of O atoms on Ni(111) are small and we shall neglect it.

The DFT calculations used to derive the lateral interaction parameters were carried out using the surface unit cells depicted in Fig. 5. Their choice was dictated by technical computing limitations (bigger cells demand too much computa-

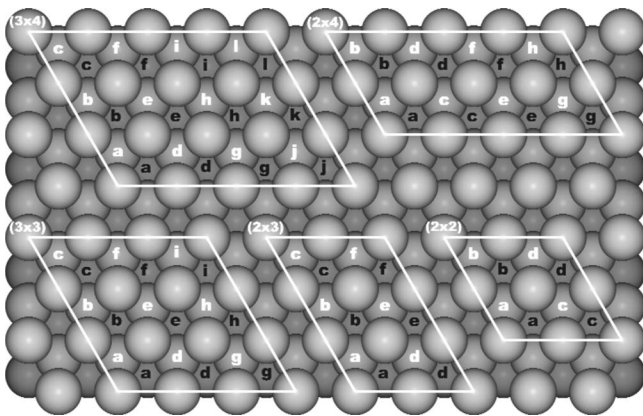


FIG. 5. Schematic illustration of the Ni(111) surface showing the different unit cells used to carry out DFT calculations for the O/Ni(111) system. The black and white letters identify the fcc and hcp sites, respectively, and are used to label each configuration in Tables V and VI.

tional resources) and compatible results among different unit cells (the unit cells \mathbf{k} -mesh grids have to be integer multiples of each other). As can be seen in Fig. 5, the biggest unit cell used is a $h(3 \times 4)$ cell, which (at the present) demands a lot of computational resources.

Since we are interested in the phase diagram of O/Ni(111) for the range $0 < \Theta \leq 0.40$ ML (at higher oxygen exposures, oxide islands form²⁶), most of the calculations have been carried out for this coverage range. Furthermore, since the fcc sites are the most stable sites, we carried out more calculations for fcc configurations than for hcp configurations. In this way, we save some computing time by excluding some configurations of the less energetically stable hcp sites.

There are many different configurations that can be calculated using the unit cells illustrated in Fig. 5. The configurations presented in Tables V and VI are a small subset of the possible configurations. This subset was selected by including the configurations predicted by the cluster expansion to be close to the ground-state line. Thus, we carried out a *ground-state search* based on *direct enumeration*⁴¹ of the different configurations that are possible to calculate within the unit cells of Fig. 5.

For the case of O/Ni(111), the ground-state search using a reduced number of configurations (10–12) led to the $p(2 \times 2)$ and the $(\sqrt{3} \times \sqrt{3})R30^\circ$ configurations as ground states for $\Theta=1/4$ ML and $\Theta=1/3$ ML, respectively. With the lateral interaction parameters derived at this stage, one then calculates the energy of *all* possible structures in the unit cells of Fig. 5, i.e., one carries out a *direct enumeration*. Those structures close to the *ground-state line* are then identified and calculated from first-principles. With this increased set of configurations, a new set of interaction parameters is derived and the latter procedure is repeated until no new structures appear close to the ground-state line.

The DFT energies of the configurations used to obtain the lateral interactions are given in Tables V and VI. Table V contains fcc and hcp configurations, while Table VI contain fcc-hcp configurations, i.e., O occupies both types of sites. To identify a specific configuration, letters have been used in Tables V and VI, which refer to the positions denoted in Fig. 5.

A close examination of the energetic data in Table V shows that E_a augments with increasing coverage. This is an indication of increasing repulsion among O atoms with increasing coverages. Table V also shows that the fcc configurations are always more favorable than the hcp configurations. However, the stability of the mixed fcc-hcp configurations (Table VI) with respect to fcc configurations increases as the coverage increases. An example of that tendency is (3×3) afh (Table V), i.e., the $(\sqrt{3} \times \sqrt{3})R30^\circ$ configuration, and (2×3) ab (Table VI), which only differ by 8 meV. In fact, for $\Theta=1/2$ ML, (2×4) afd in Table VI is energetically more favorable than all fcc configurations in Table V.

Thus, as the coverage increases (and with it, the repulsive interaction), the O atoms try to diminish their repulsive interactions by partially occupying hcp sites. Energetically, the occupation of hcp sites instead of fcc sites is unfavorable; however, the reduction in repulsive lateral interactions makes it possible. We shall see that this fact has significant effects on the O/Ni(111) phase diagram.

TABLE V. E_a per atom for different fcc and hcp configurations of O atoms on Ni(111) obtained from DFT calculations. The letters denote the position of O atoms in every unit cell according to the nomenclature illustrated in Fig. 5.

Unit cell	Θ (ML)	Config.	E_a^{fcc} (eV)	E_a^{hcp} (eV)
(2×2)	1/4	a	-2.877	-2.750
	1/2	ab	-2.404	-2.274
	3/4	abc	-1.955	-1.804
	1	abcd	-1.423	-1.273
$(2 \times 3)^a$	1/6	a	-2.853	-2.740
	1/3	ab	-2.666	
	1/3	ae	-2.635	
	1/3	ad	-2.393	
	1/2	abf	-2.391	
	1/2	abe	-2.307	
	2/3	abde	-2.092	
	2/3	abcd	-2.083	
	2/3	abef	-2.064	
	5/6	abcde	-1.766	
(2×4)	1/8	a	-2.854	-2.758
	1/4	af	-2.817	-2.700
	1/4	ac	-2.673	
(3×3)	1/9	a	-2.833	-2.709
	2/9	af	-2.785	-2.669
	2/9	ae	-2.666	-2.548
	1/3	afh	-2.750	-2.625
	1/3	aef	-2.558	
	2/3	acefgh	-2.082	-1.943
(3×4)	1/12	a	-2.843	-2.728
	1/6	ah	-2.824	-2.704
	2/9	ae	-2.666	-2.548
	2/9	af	-2.820	
	1/4	afh	-2.793	

^aThe configurations calculated in the (2×3) unit cell for which $\Theta \geq 1/2$ ML were carried out using $R_{\text{MT}}^{\text{O}}=1.3$ bohr and $E_{\text{max}}^{\text{wf}}=16$ Ry, because, after relaxing those structures, the muffin-tin spheres overlap if $R_{\text{MT}}^{\text{O}}=1.4$. The formation energies of those structures were calculated from Eq. (7). From those results, the E_a energies reported above were obtained from Eq. (8).

Despite the fact that Ni oxide is formed for $\Theta > 0.4$ ML,²⁶ the set of configurations in Tables V and VI does comprise structures with coverages up to 1 ML, since these structures are required during the derivation of lateral interactions to determine, in particular, the higher-order many-body interactions occurring in (locally) denser adatom arrangements. A similar inclusion of structures has been done to calculate lateral interaction parameters for O/Pd(100), where at $\Theta > 0.5$ ML, O readily incorporates inside the substrate.⁷⁸

TABLE VI. E_a per atom for different fcc-hcp configurations of O atoms on Ni(111) obtained from DFT calculations. The letters denote the position of O atoms in every unit cell according to the nomenclature illustrated in Fig. 5.

Unit cell	Θ (ML)	fcc	hcp	$E_a^{\text{fcc-hcp}}$ (eV)
(2×2)	1/2	a	d	-2.392
	1/2	a	a	+3.521
(2×3)	1/3	a	b	-2.742
	1/3	a	f	-2.641
	1/2	ae	f	-2.445
	1/2	ab	f	-2.379
(2×4)	1/4	a	f	-2.773
	1/4	a	g	-2.768
	1/2	af	gd	-2.476
(3×3)	2/9	a	h	-2.746
	1/3	af	h	-2.768
(3×4)	1/4	ag	b	-2.781
	1/4	ak	i	-2.750
	1/3	ah	bi	-2.720

The E_a energies of the different configurations in Tables V and VI are plotted in Fig. 6. The E_a energies decrease with coverage and level off at low coverages ($\Theta < 1/6$) ML—an indication that after some distance the O atoms do not appreciably interact. This fact leads us to conclude that we do not need long distance interactions in our Hamiltonian [Eq. (4)].

The formation energies are plotted in Fig. 6. The DFT ground-state line is shown for $0 \leq \Theta \leq 1/2$ ML, which is the coverage range for which most of the DFT calculations have been carried out. As noted in Fig. 6, the $p(2 \times 2)$ and the $(\sqrt{3} \times \sqrt{3})R30^\circ$ configurations are the ground states at $\Theta = 1/4$ and $1/3$ ML, respectively, in agreement with experiments.^{17,18}

B. Lateral interaction parameters

The values of the ECIs for different genetic-algorithm optimizations are depicted in Table VII under cases II–IV. The candidate ECIs have been chosen using the maximal cluster concept.^{29,48} Interactions beyond trios (e.g., quartets and quintets) are not included. At the low-coverage range of the O/Ni(111) phase diagram ($0 < \Theta \leq 0.40$) ML, we do not expect the O atoms to frequently form dense clusters, i.e., the frequency of multisite interactions should be low.

Statistical data are given for every case in Table VII. The statistics reported are the average of the absolute value of the residuals $|y_i - \hat{y}_i|_{\text{avg}}$ (where y_i is the DFT E_a and \hat{y}_i is E_a given by the Hamiltonian), an estimator of the error variance $\hat{\sigma}^2$ (also known as the mean square error), cross-validation score CV, Mallows's C_p statistics, coefficient of determination R^2 ,

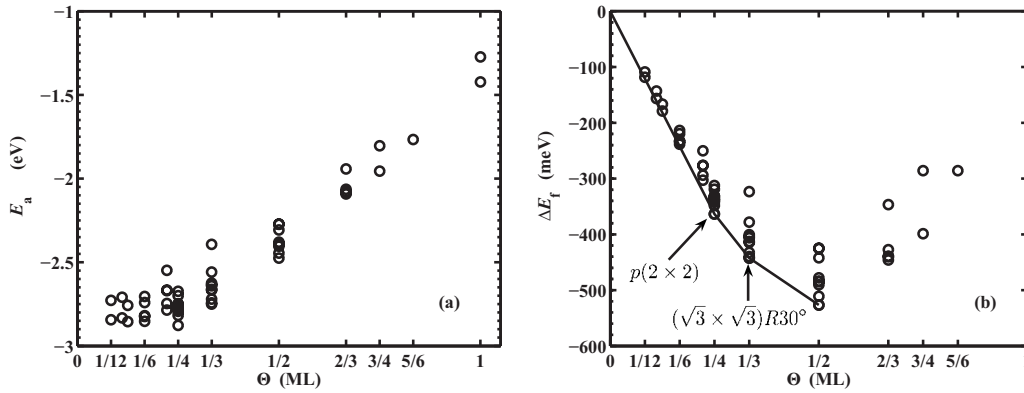


FIG. 6. (a) DFT E_a energies (per atom) plotted against coverage Θ . The E_a data levels off at the *zero coverage limit* for low coverages. A total of 56 different configurations have been calculated and are listed in Tables V and VI. (b) DFT formation energies ΔE_f (per site) plotted against coverage Θ , and the DFT ground-state line for $0 \leq \Theta \leq 1/2$. The configurations corresponding to the ground-state structures at $\Theta = 1/4$ and $1/3$ ML are annotated with arrows.

adjusted coefficient of determination R_{adj}^2 , and the number of parameters.

No optimization criterion was used in the parameter set of case I. This set shows the interaction energies corresponding to the “obvious” ECIs, i.e., close range interactions. The same interactions were used in Refs. 14 and 16. They include the pair and trio interactions depicted in Fig. 2 plus three pair fcc-hcp interactions. Case I also shows 95% confidence intervals (CIs) for the energy parameters.⁷⁹ Cases II, III, and IV are the result of optimizing CV, C_p statistics, and R_{adj}^2 , respectively.

The values of the parameters are very similar from case to case. The pair interactions tend to decrease with distance and are mostly positive (indicating mostly repulsive interactions). The value of the fcc V_{p3} parameter is always negative. This is an indication that the $p(2 \times 2)$ is very stable, since that is the pair interaction present in that phase. The value of the fcc-hcp V_{p1} parameter is very large and indicates that O atoms repel each other very strongly at short distances.

The trio interactions are of the same order of magnitude as the pair interactions. In particular, V_{t3} has a very high negative (attractive) value. This high value is mostly a counterbalance of the high positive (repulsive) value of V_{p1} (which is always present whenever V_{t3} is present). Case II (CV) shows that the fcc triangular trio interactions V_{t3} (nearest neighbors), V_{t4} (second-nearest neighbors), and V_{t5} (third-nearest neighbors), when included, tend to decrease with interaction distance.

The energy difference between fcc and hcp adsorption sites (≈ 100 meV; see fcc V_0 and hcp V_0) is in the same energy range of the pairs and trios. This is another indication that O can occupy hcp sites when trying to minimize the repulsive interactions at increased coverages.

The parameter set obtained from the CV optimization does not include fcc V_{p2} . This is counterintuitive since one would expect fcc V_{p2} to play an important role in the $(\sqrt{3} \times \sqrt{3})R30^\circ$ phase at $\Theta = 1/3$ ML (where the interactions are given by second-nearest neighbors). That interaction, however, is partially accounted for in case II (CV) by including V_{t4} (the triangular trio formed by second-nearest neighbors). The omission of a physically important interaction parameter

illustrates the tendency of the CV score to render the optimized ECIs as purely stochastic variables.⁵² The other two optimizing criteria, C_p statistics and R_{adj}^2 , include V_{p2} .

The $p(2 \times 2)$ order-disorder phase transitions calculated from the interaction parameters in Table VII are illustrated in Fig. 7. The phase transitions were identified by canonical Monte Carlo simulations as the inflection point of the $p(2 \times 2)$ order parameter [Eq. (12)] plotted against the temperature for constant coverage.

The phase transition corresponding to the fcc only parameters of case I has been included in Fig. 7 as well. For this set, i.e., case I: fcc parameters, we obtain the highest transition temperatures. Including the corresponding hcp parameters, i.e., case I, decreases the transition temperatures by about 150 K. This is reasonable since by additionally including the hcp sites in the lattice, the configuration space of the O atoms increase (the configurational entropy increases). Thus, the tendency to disorder of the O atoms increases, i.e., the order-disorder transition temperatures decrease.

The transition temperatures resulting from the extreme values of the 95% confidence intervals of case I are also illustrated in Fig. 7. The transition temperatures vary within a range of $\Delta T \approx 100$ K. Thus, the statistical uncertainty of the ECI parameters of case I leads to a fairly small variation range for the transition temperatures of O/Ni(111). Consequently, one can reasonably expect that the ideal phase diagram (obtained from a direct coupling of DFT energies with Monte Carlo) would lie very close to the phase diagram calculated by the cluster expansion Hamiltonian.⁸⁰

The optimized parameter sets, i.e., cases II–IV, lead to essentially the same transition temperatures for $\Theta = 1/4$ ML. Those critical temperatures lie in the lower extreme of the 95% confidence interval of case I. Small variations are present in the transition temperatures of cases II–IV for $\Theta < 1/4$ ML.

The different ECI sets of Table VII lead to very similar $p(2 \times 2)$ transition temperatures for O/Ni(111). We have not tested the different ECI sets with respect to other transitions [testing of the $(\sqrt{3} \times \sqrt{3})R30^\circ$ transition at $\Theta = 1/3$ ML would require lengthy Wang-Landau simulations for every set because of the strong first-order nature of this transition]. How-

TABLE VII. ECIs and scores obtained from genetic-algorithm fits of the cluster expansion [Eq. (4)] to the DFT energies in Tables V and VI. The ECIs are given in (meV). The cluster figures corresponding to each ECI are denoted by letters referred to the (3×4) unit cell in Fig. 5.

Site	ECI ^a	Position	Cases				
			I	II (CV)	III (C_p)	IV (R_{adj}^2)	
fcc	V_0	a	-2832.3 ± 10.7	-2833.1	-2837.8	-2847.0	
	V_{p1}	ab	348.5 ± 16.7	328.1	351.2	329.2	
	V_{p2}	af	26.5 ± 7.5		29.0	26.6	
	V_{p3}	ac	-14.8 ± 7.4	-25.9	-10.5	-7.8	
	V_{p4}	ak		17.6		7.4	
	V_{p5}	aj		5.9		4.8	
	V_{i1}	abc	91.0 ± 18.4	81.9	102.0	101.0	
	V_{i2}	abf	59.1 ± 11.1	54.4	69.4	68.8	
	V_{i3}	abe	-158.0 ± 33.7	-153.9	-172.8	-170.8	
	V_{i4}	afh		32.3			
	V_{i5}	aig		19.6			
	V_{i6}	afi			-7.3	-5.7	
	hcp	V_0	a	-2720.5 ± 13.2	-2742.9	-2743.4	-2742.7
		V_{p1}	ab	343.2 ± 39.8	340.6	340.3	340.3
		V_{p2}	af	31.2 ± 8.8	32.7	32.2	32.2
		V_{p3}	ac	-11.9 ± 9.3			
V_{p4}		ak					
V_{p5}		aj		9.0	9.5	9.2	
V_{i1}		abc	96.2 ± 47.6				
V_{i2}		abf	61.5 ± 24.4	15.2	15.1	15.3	
V_{i3}		abe	-150.9 ± 83.6				
V_{i4}		afh					
V_{i5}		aig					
V_{i6}		afi		19.2	19.4	19.3	
fcc-hcp ^b		V_{p1} ^c	aa	12616.2 ± 61.1	12561.4	12563.1	12563.9
		V_{p2}	ab	282.3 ± 13.7	276.2	276.7	275.5
		V_{p3}	af	29.4 ± 10.1	20.8	24.6	22.7
		V_{p4}	ac		26.6	21.2	22.9
	V_{p5}	ak					
	V_{p6}	aj					
		$ y_i - \hat{y}_i _{\text{avg}}$	8.4	8.1	7.4	7.0	
		$\hat{\sigma}^2$	160.1	155.6	114.6	111.9	
		CV	21.9	15.2	16.6	16.3	
		C_p statistics	24.2	25.4	11.9	13.5	
		R^2	0.99915	0.99924	0.99941	0.99945	
		R_{adj}^2	0.99883	0.99886	0.99916	0.99918	
	No. param.	17	20	18	20		

^aThe fcc, hcp and fcc-hcp ECIs were fitted simultaneously to the E_a results reported in Tables V and VI. Thus, we did not decouple the system of equations as was done in Ref. 14.

^bfcc-hcp denotes cluster figures containing both fcc and hcp sites. Formally, one should consider the tensor product of fcc and hcp clusters (Refs. 27 and 39). However, we have only considered the pairs of that product. Thus, the first and second letters in the column position for fcc-hcp denote fcc and hcp positions, respectively, in the (3×4) unit cell in Fig. 5.

^cThe energetic value of the fcc-hcp pair nearest-neighbor interaction is very high and can lead to numerical instabilities in the genetic-algorithm optimizations. Thus, this parameter was not included in the optimizations. Once the other ECIs participating in the expansion were known, the value of fcc-hcp V_{p1} was derived from the $(2 \times 2)_{\text{a}^{\text{fcc}}-\text{a}^{\text{hcp}}}$ configuration in Table VI.

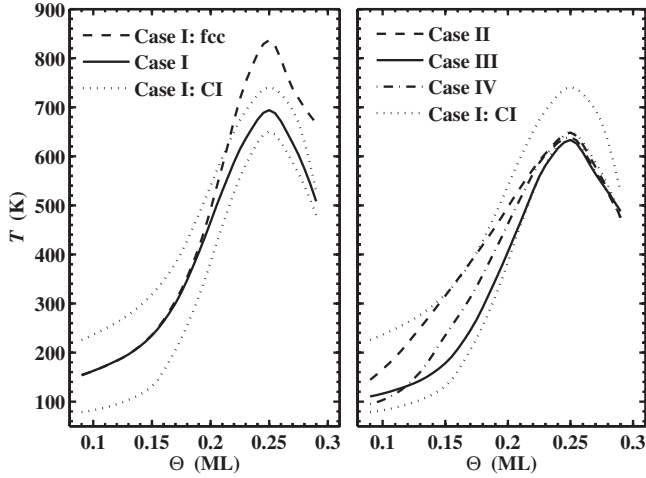


FIG. 7. $p(2 \times 2)$ order-disorder phase transition calculated for the different parameter sets in Table VII. The acronym CI refers to the 95% confidence intervals of case I.

ever, ECIs that are important to other phases are implicitly considered in the $p(2 \times 2)$ transition. The ground state and the specific location of the transition temperature for $1/4 < \Theta < 1/3$ ML are the result of the relative stability of $p(2 \times 2)$, $(\sqrt{3} \times \sqrt{3})R30^\circ$, and any other stable phase [e.g., antiphase $p(2 \times 2)$ domains¹⁸]. The fact that the $p(2 \times 2)$ transition is very similar for the different fcc-hcp sets of Fig. 7 means that the other transitions have a similar relative stability for the different sets. This argument is plausible for phases that coexist due to their coverages being close (e.g., like the phases at $\Theta = 1/4$ and $1/3$ ML).

The results depicted in Fig. 7 were obtained without including mixed (fcc-hcp) multisite interactions (only mixed pairs were included). One can reasonably expect that mixed fcc-hcp multisite interactions would be important in the Hamiltonian of a fcc-hcp adsorption system. However, their inclusion would significantly complicate the calculations. In view of the good reproducibility of the DFT energies by the different parameter sets in Table VII (small residuals average) and the similarity of the phase-transition lines in Fig. 7, we expect that our expansion reproduces fairly well the phase diagram that one would obtain by directly coupling Monte Carlo simulations with DFT calculations.

For the calculation of the thermodynamic properties and the remaining parts of the O/Ni(111) phase diagram, we shall use case III (C_p) of Table VII, i.e., the parameter set obtained from optimizing C_p statistics. Our choice is based on the fact that the CV score tends to render the optimized ECIs as purely stochastic variables (as has been discussed above), and the C_p criterion is statistically more meaningful than R_{adj}^2 .

C. Thermodynamic properties

Once the O/Ni(111) ECI parameters have been determined from first-principles, one can carry out Monte Carlo simulations in order to study the thermal behavior of the system. Figure 8 shows a selection of calculated thermody-

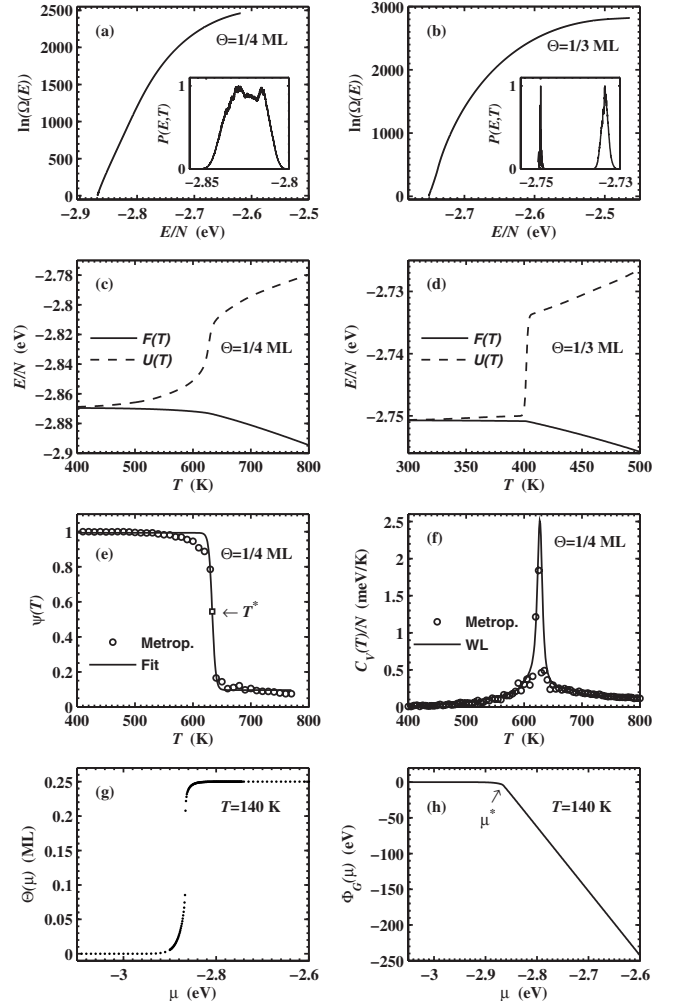


FIG. 8. Thermodynamic properties of the O/Ni(111) system calculated from Metropolis and Wang-Landau Monte Carlo simulations. (a) Logarithm of the configurational density of states $\ln[\Omega(E)]$ against the energy per atom (N is the number of atoms) for $\Theta = 1/4$ ML. The inset shows the normalized canonical distribution at the transition temperature $P(E, T^*) = \Omega(E)e^{-E/k_B T^*}$. (b) Configurational density of states and canonical distribution for $\Theta = 1/3$ ML. (c) Helmholtz free energy $F(T)$ and internal energy $U(T)$ for $\Theta = 1/4$ ML. (d) $F(T)$ and $U(T)$ for $\Theta = 1/3$ ML. (e) Metropolis Monte Carlo simulation results for the $p(2 \times 2)$ order parameter $\psi(T)$, calculated according to Eq. (12), for $\Theta = 1/4$ ML and sigmoidal fit to the data. The transition temperature T^* is given by the inflection point of the sigmoidal fit. (f) Comparison of heat capacity $C_V(T)$ results from Metropolis and Wang-Landau Monte Carlo simulations for $\Theta = 1/4$ ML. (g) Dependence of the coverage Θ on the chemical potential μ at $T = 140$ K as obtained from Metropolis Monte Carlo simulations in the grand canonical ensemble. (h) Grand canonical potential Φ_G versus chemical potential μ at $T = 140$ K obtained from integration of Eq. (14). The location of the chemical potential of the transition, μ^* , is given by the discontinuity of the first derivative of the $\Phi_G(\mu)$ curve.

amic properties for $\Theta = 1/4$ and $1/3$ ML as obtained from Metropolis and Wang-Landau simulations. Figures 8(a)–8(d) are the result of Wang-Landau Monte Carlo simulations; Figs. 8(e), 8(g), and 8(h) were obtained from Metropolis

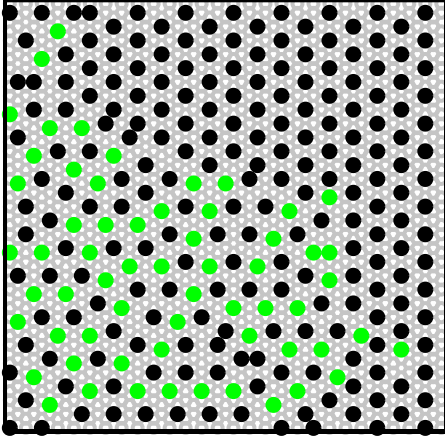


FIG. 9. (Color online) Snapshot of the $(\sqrt{3} \times \sqrt{3})R30^\circ$ first-order transition at $\Theta=1/3$ ML. Black (black) and gray (green) circles indicates O atoms occupying fcc and hcp sites, respectively.

Monte Carlo simulations; while Fig. 8(f) compares results obtained from both algorithms.

The nature of the phase transitions (first order or continuous) at $\Theta=1/4$ and $1/3$ ML has been investigated by calculating their canonical distributions $P(E, T^*) = \Omega(E) e^{-E/k_B T^*}$, where T^* is the temperature at the phase transition. The distributions have not been obtained from Metropolis Monte Carlo simulations of the system close to the phase transition (since, in doing so, previous results showed the failure⁸¹ or the inaccuracy⁸² of employing the calculated canonical distribution to determine the nature of the phase transition). They have been calculated from the configurational density of states, $\Omega(E)$. Instead of trying to extract $\Omega(E)$ from the probability distribution produced by “standard” Monte Carlo simulations,^{81,82} the Wang-Landau algorithm (used here) estimates $\Omega(E)$ directly. By shifting the acceptance rule in the Monte Carlo simulation from energy to entropy space, the Wang-Landau algorithm is able to surmount the problem posed by hysteresis at first-order phase transitions and critical slowing down at continuous phase transitions. The algorithm has shown that it is able to sample very complex energy profiles accurately.^{33,34,54}

The phase transition at $\Theta=1/3$ ML [that is, the $(\sqrt{3} \times \sqrt{3})R30^\circ$ transition] clearly exhibits all the characteristics of a first-order transition: a double-peaked canonical probability distribution at the transition temperature T^* indicating the coexistence of two phases at the transition [Fig. 8(b)], a steplike change in the energy, and a discontinuity at the Helmholtz free energy [Fig. 8(d)]. Experimental studies^{17–19} have also found that O/Ni(111) exhibits a first-order $(\sqrt{3} \times \sqrt{3})R30^\circ$ transition.

A snapshot of the $(\sqrt{3} \times \sqrt{3})R30^\circ$ phase transition obtained from Monte Carlo simulations is depicted in Fig. 9. Two coexisting phases, $(\sqrt{3} \times \sqrt{3})R30^\circ$ and a disordered phase, can clearly be identified. The O atoms in the $(\sqrt{3} \times \sqrt{3})R30^\circ$ phase occupy only fcc sites; while in the disordered phase, they occupy both fcc and hcp sites. The increased energetic stability of mixed fcc-hcp configurations with increased coverage discussed in Sec. IV A plays already

a role at $\Theta=1/3$ ML. Thus, the increased energetic competition of fcc-hcp configurations is the microscopic cause of the $(\sqrt{3} \times \sqrt{3})R30^\circ$ phase exhibiting a first-order transition.

Because of the double-peaked structure at the first-order $(\sqrt{3} \times \sqrt{3})R30^\circ$ phase transition, Metropolis canonical Monte Carlo simulations are not efficient because an extremely long time is required for the system to travel from one peak to the other in energy space. Thus, strong hysteresis effects are present [LEED experiments also have found strong hysteresis at the $(\sqrt{3} \times \sqrt{3})R30^\circ$ transition¹⁷]. The Wang-Landau algorithm allows the simulation to access all energy levels with equal probability (random walk in energy space). So it overcomes the barrier between the coexisting phases and allows for an accurate evaluation of the transition temperature.

The nature of the $p(2 \times 2)$ transition at $\Theta=1/4$ ML is more subtle. To date, different experimental results about the nature of this transition have disagreed. Roelofs *et al.*²² found the transition to be continuous Ising-like, Li *et al.*²⁴ found a continuous four-state Potts-like transition, while Schwenger *et al.*²³ and Voges and Pfnür⁸³ found the transition to be weakly first order. Likewise, Monte Carlo simulations have been inconclusive about the nature of this phase transition.⁸¹

A close look at the canonical distribution in Fig. 8(a) suggests that the $p(2 \times 2)$ transition at $\Theta=1/4$ ML is of weakly first-order character. The double peak structure is not as evident as was the case for the $(\sqrt{3} \times \sqrt{3})R30^\circ$ transition [Fig. 8(b)]; however, the distribution shows two peaks instead of one (as it would be the case of a continuous phase transition). This result about the nature of the $p(2 \times 2)$ transition is by no means conclusive since we have not calculated the critical exponents of the $p(2 \times 2)$ transition. This will be the subject of a subsequent paper.

The $p(2 \times 2)$ transition can also be accurately determined by Metropolis canonical Monte Carlo simulations. Figure 8(e) shows the results of Metropolis Monte Carlo simulations for the $p(2 \times 2)$ order parameter and the sigmoidal fit used to determine the transition temperature. Figure 8(f) shows the results of both Monte Carlo methods for the heat capacity. The results are in excellent agreement and also show the same transition temperature (the peak of the curve) as the $p(2 \times 2)$ order parameter. In fact, determining the transition temperature by the point of inflection in the order-parameter curve and by the maximum in the heat capacity curve are closely related.⁸⁴

Figure 8(g) shows an example of the Metropolis grand canonical Monte Carlo simulation results used to determine phase coexistence. The discontinuous jump in the $\Theta(\mu)$ curve indicates a first-order transition. The location of the chemical potential of the transition is carried out by finding the discontinuity point (intersection point) in the grand canonical potential versus chemical-potential curve [Fig. 8(h)]. Scans similar to the one shown in Figs. 8(g) and 8(h) were carried out in order to calculate the phase-coexistence boundaries in the simulated O/Ni(111) phase diagram of Fig. 10.

D. O/Ni(111) phase diagram

The calculated equilibrium phase diagram of O/Ni(111) as calculated from Monte Carlo simulations is illustrated in Fig.

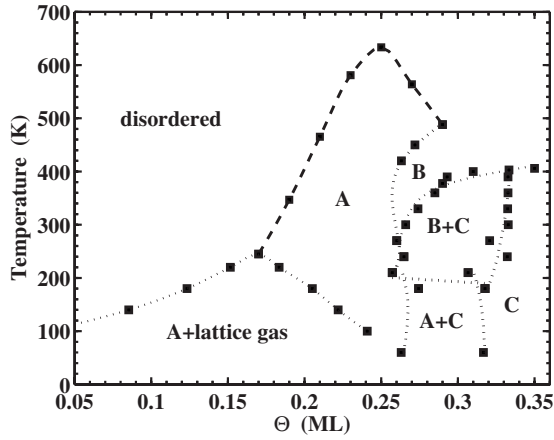


FIG. 10. Phase diagram of O/Ni(111) as calculated from Monte Carlo simulations. The dotted lines denote first-order phase transition while the dashed lines denote weakly first-order or continuous phase transitions. Pure phases and phase-coexistence regions are identified with letters that make reference to the snapshots in Fig. 11.

10. The dotted lines denote first-order transitions and the dashed lines denote weakly first-order or continuous transitions (see discussion in the last section). Snapshots of the different phases are illustrated in Fig. 11.

All phases present in the experimental phase diagram (Fig. 1) are present in our theoretical phase diagram. Besides, we also obtained a $p(2 \times 2) + (\sqrt{3} \times \sqrt{3})R30^\circ$ coexistence region (denoted by A+C). This region has not been observed in experiments yet (probably due to low mobility of oxygen at low temperatures), but it has been postulated in an empirical fitting of interaction parameters to the experimental O/Ni(111) phase diagram.¹⁸

The so-called antiphase (phase B in Figs. 10 and 11) is made of $p(2 \times 2)$ domains, with oxygen in fcc sites, separated by a random distribution of domain walls in which hcp sites are occupied. The antiphase is not a ground state of the O/Ni(111) system but exists only as a thermally activated phase. The ground states are the $p(2 \times 2)$ phase (either pure or coexisting with a lattice gas), the $(\sqrt{3} \times \sqrt{3})R30^\circ$ phase, and a coexistence of $p(2 \times 2) + (\sqrt{3} \times \sqrt{3})R30^\circ$ phases. Those ground states are the same states given by the DFT ground-state line in Fig. 6(b).

Thus, qualitatively, our O/Ni(111) phase diagram from first-principles closely matches the LEED experimental phase diagram.^{17,18} Additionally, our Monte Carlo Simulations based on first-principles are able to resolve the ground state for $1/4 > \Theta > 1/3$ ML, i.e., the $p(2 \times 2) + (\sqrt{3} \times \sqrt{3})R30^\circ$ phase.

Differences arise in the transition temperature values. The theoretical phase diagram predicts transition temperatures

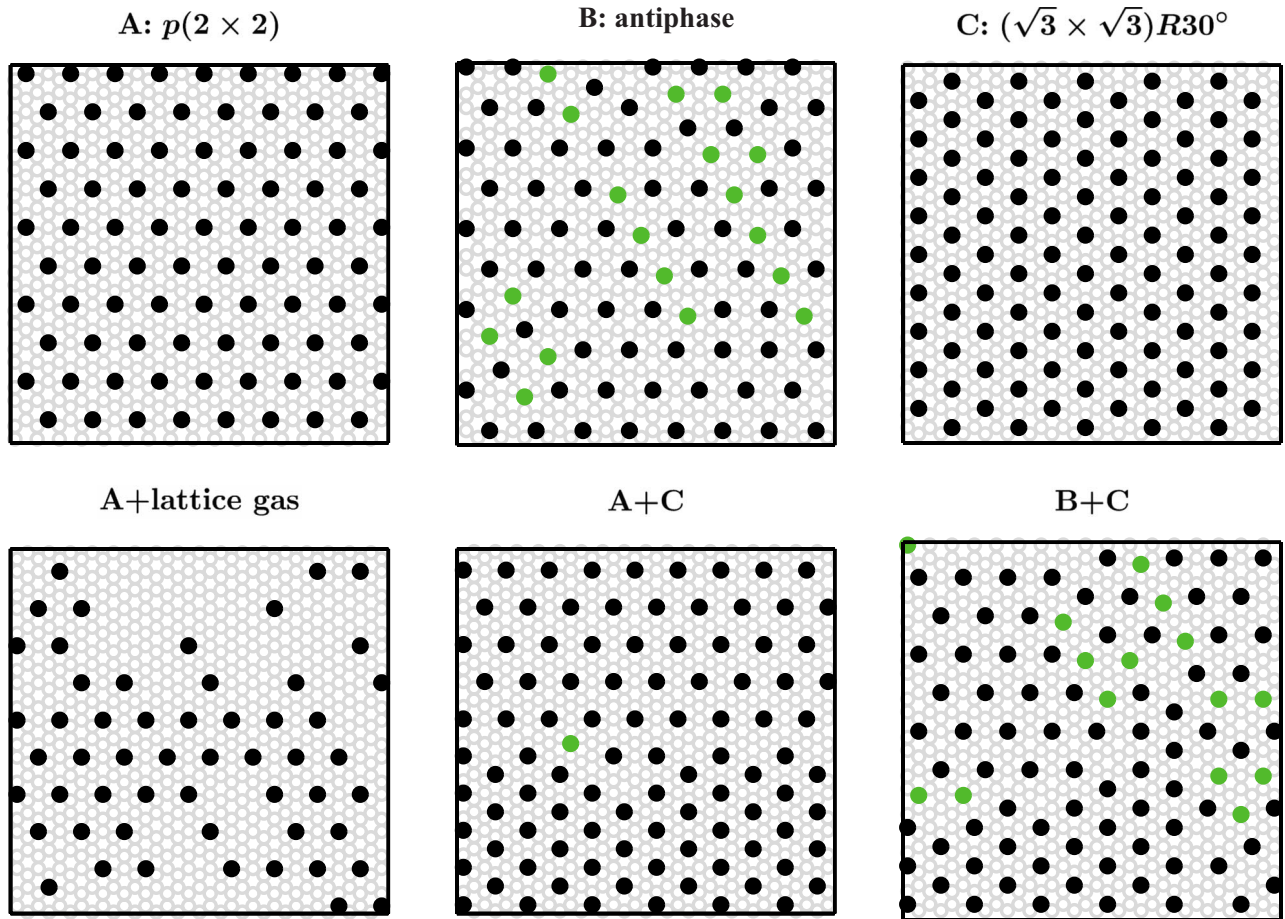


FIG. 11. (Color online) Snapshots of pure phases and phase-coexistence configurations of O/Ni(111). Black (black) and gray (green) circles denote O adsorbed on fcc and hcp sites, respectively. The letters denote stability regions in Fig. 10.

TABLE VIII. Order-disorder transition temperatures for the $p(2 \times 2)$ phase at $1/4$ ML and the $p(2 \times 2) + (\sqrt{3} \times \sqrt{3})R30^\circ$ phase at $1/3$ ML obtained from LEED experiments (Ref. 18) and first-principles Monte Carlo simulations. The same differences (100–200 K) between experimental and theoretical results have also been found in the case of O/Ru(0001) (Ref. 12).

	$p(2 \times 2)$	$(\sqrt{3} \times \sqrt{3})R30^\circ$	Ratio
T_{Expt} (K)	440	314	1.4
T_{MC} (K)	623	404	1.5

higher than the experimental ones (see Table VIII). However, the *ratio* of the transition temperatures at $\Theta=1/4$ and $1/3$ ML is essentially the same, i.e., the relative thermal stability of the $p(2 \times 2)$ and $(\sqrt{3} \times \sqrt{3})R30^\circ$ phases in both diagrams is very similar. This is one more indication of the excellent qualitative agreement of both phase diagrams.

In our model of the O/Ni(111) system we neglected subsurface occupation and vibrational entropy. Those additional degrees of freedom would further reduce the calculated transition temperatures. However, as explained in Sec. IV A, we do not expect major changes in the transition temperatures by including them in our model.

Further insight into the reasons behind the temperature mismatch can be obtained by comparing spillover data for $\Theta=1/4$ ML from LEED experiments²⁵ and our calculations (see Fig. 12). Our Monte Carlo simulations (case III in Fig. 12) predict a reduced spillover onto hcp sites when compared to the experimental data. This leads to increased transition temperatures because fcc adsorption, i.e., the $p(2 \times 2)$ phase, is predicted to be more stable than what one observes in experiments.

Schwennicke and Pfnür¹⁸ estimated the energy difference between fcc and hcp sites and obtained a value of 46 meV. In comparison, our cluster expansion predicts a E_a difference of 94 meV (from V_0^{fcc} and V_0^{hcp} in Table VII). If we take $V_0^{\text{hcp}} - V_0^{\text{fcc}} = 46$ meV, we obtain a better agreement with the

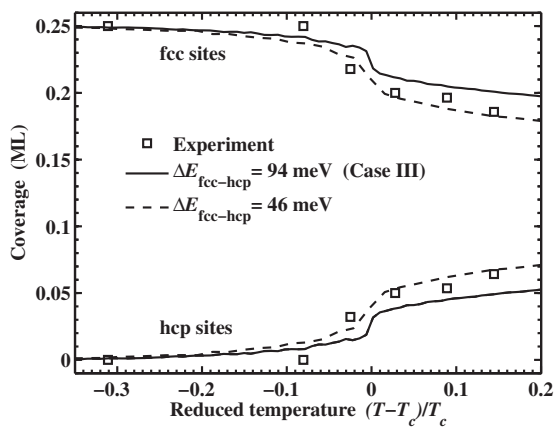


FIG. 12. Experimental data points of coverage in fcc and hcp sites for $\Theta=1/4$ ML as a function of the reduced temperature $(T - T_c)/T_c$ obtained by analyzing LEED $I(E)$ curves (Ref. 25). The results of Monte Carlo simulations are shown for comparison. Both experiment and simulations produce an S-shaped curve with a maximum slope at the transition temperature.

experimental data (see Fig. 12). In view of this result, one could think that our DFT calculations predict an overbinding to fcc sites; however, the value obtained by Schwennicke and Pfnür and ours are not directly comparable because Schwennicke and Pfnür used a completely different setup considering only pair interactions; in addition, only relative values were determined and then fitted to experiment.¹⁸ The reduced spillover onto hcp sites obtained from our simulations is the result of the interplay among all ECIs we have considered in the simulations and not only of the energy difference between fcc and hcp sites. Thus, most probably, the overall accuracy of DFT is responsible for this discrepancies.

All in all, the calculated O/Ni(111) phase diagram nicely reproduces the qualitative features of the experimental one and lead to transition temperatures in the same order of magnitude of the experimental ones. Closer agreement seems to depend on improvement in the accuracy of the exchange and correlation functionals of DFT theory.

V. CONCLUSIONS

We have thoroughly studied the phase diagram of O adsorbed on Ni(111) based only on input from DFT calculations. Different statistical criteria coupled with a genetic-algorithm search have been used in order to derive the lateral interactions from DFT calculations. We have chosen the C_p statistics which gave reasonable coefficients. We recommend a comparison of the results from different statistical approaches as there is no general rule about which method is the best. We showed that for the case of O/Ni(111), it is necessary to include both fcc and hcp adsorption sites in the simulation of the phase diagram.

The thermodynamic properties and the surface phase diagram of the O/Ni(111) system have been calculated from Monte Carlo simulations using the Metropolis and Wang-Landau algorithms. Canonical distributions, obtained from Wang-Landau Monte Carlo simulations, clearly showed a first-order phase transition at $\Theta=1/3$ ML in agreement with previous experiments and calculations. Our results for the $p(2 \times 2)$ phase transition at $\Theta=1/4$ ML suggest a weakly first order-transition. However, this result is by no means conclusive and we still need to calculate the critical exponents of the $p(2 \times 2)$ transition in order to figure out its nature. To date, there is no agreement in the literature about the nature of this transition.

The calculated O/Ni(111) phase diagram agrees qualitatively very well with the experimental one. All phases that have been experimentally determined are present in our simulated phase diagram. Additionally we found a coexistence region of $p(2 \times 2)$ and $(\sqrt{3} \times \sqrt{3})R30^\circ$ phases at very low temperatures. Due to adsorbate mobility, low-temperature coexistence regions are very difficult to be detected experimentally. The $p(2 \times 2)$ antiphase found in experiments is, according to our results, not a ground-state phase but a thermally activated one.

Differences arise in the values of the transition temperatures. Our theoretical transition temperatures are 100–200 K higher than the experimental ones. We were able to determine that our simulations predict a spillover onto hcp sites

that is less than in the experimental data. This leads to increased transition temperatures since fcc adsorption is predicted to be more stable than what one observes in experiments. The reduced spillover obtained in our results is a consequence of the interplay among all interactions considered in the simulations. Most probably, the overall accuracy of DFT is responsible for this discrepancies. Thus, improvement in the calculation of O/Ni(111) transition temperatures based on DFT calculations demands more accurate DFT exchange and correlation functionals.

ACKNOWLEDGMENTS

We gratefully thank John Kitchin at Carnegie Mellon University and Emily Carter at Princeton University for critical reading of the manuscript and their valuable comments. The use of computing facilities at the Hamburg University of Technology and University of Hamburg is also gratefully acknowledged.

APPENDIX

Table IX shows formation energies [calculated by using Eq. (8)] for $\Theta=1/4$ ML in a (2×2) unit cell. The energies were calculated for different layers of Ni in the supercell and for adsorption of O on fcc and hcp sites. The vacuum between subsequent slabs was 15 Å for every calculation. The results show that a five layer slab model leads to well-converged values of the formation energies. Since these are

TABLE IX. Calculated formation energies ΔE_f^Θ for $\Theta=1/4$ ML in a (2×2) unit cell. Both fcc and hcp occupation sites have been calculated.

Ni layers	$\Delta E_{f(\text{fcc})}^{1/4\text{ML}}$ (meV)	$\Delta E_{f(\text{hcp})}^{1/4\text{ML}}$ (meV)
3	-340	-334
5	-364	-332
7	-366	-335
9	-362	-337
11	-363	-334

the central quantities determining the stability of the difference phases present in the system, a five layer slab model is fine for studying the phase diagram of O/Ni(111).

The number of layers in the slab necessary to study a specific system varies from system to system. For example, Stasevich *et al.*⁸⁵ found that a seven layer slab (both sides adsorption) was necessary to study the interactions of Cu on Cu(111) and Cu(001), while Tiwary and Fichtorn⁸⁶ found that a ten layer slab (one side adsorption) was essential to study the interaction between Al atoms on Al(110). On the other hand, Stampfl and Scheffler⁸⁷ used a four layer slab (one side adsorption) to study the interactions of O on Ru(0001), Tang *et al.*¹⁶ used a three layers slab (one side adsorption) to study the phase diagram of O/Pt(111), and Zhang *et al.*⁷⁸ used a five layer slab (both sides adsorption) to study the phase diagram of O/Pd(100).

*Corresponding author; clazo@physnet.uni-hamburg.de

¹W. H. Weinberg, *Annu. Rev. Phys. Chem.* **34**, 217 (1983).

²E. Bauer, in *Structure and Dynamics of Surfaces*, edited by W. Schommers and P. von Blanckenhagen (Springer, Berlin, 1987), Vol. II, p. 115.

³B. N. J. Persson, *Surf. Sci.* **15**, 1 (1992).

⁴L. D. Roelofs, in *Handbook of Surface Science*, edited by W. N. Unertl (Elsevier, Amsterdam, 1996), Vol. 1, p. 713.

⁵L. D. Roelofs and P. J. Estrup, *Surf. Sci.* **125**, 51 (1983).

⁶K. Binder and D. P. Landau, in *Molecule Surface Interactions*, edited by K. P. Lawley (Wiley, Chichester, 1989), p. 91.

⁷J. Trost, T. Zambelli, J. Winterlin, and G. Ertl, *Phys. Rev. B* **54**, 17850 (1996).

⁸L. Österlund, M. O. Pedersen, I. Stensgaard, E. Lægsgaard, and F. Besenbacher, *Phys. Rev. Lett.* **83**, 4812 (1999).

⁹P. Hohenberg and W. Kohn, *Phys. Rev.* **136**, B864 (1964).

¹⁰W. Kohn and L. J. Sham, *Phys. Rev.* **140**, A1133 (1965).

¹¹R. G. Parr and W. Yang, *Density Functional Theory* (Oxford University Press, New York, 1989).

¹²J.-S. McEwen, S. H. Payne, and C. Stampfl, *Chem. Phys. Lett.* **361**, 317 (2002).

¹³H. Tang, A. Van der Ven, and B. L. Trout, *Phys. Rev. B* **70**, 045420 (2004).

¹⁴C. Stampfl, H. J. Kreuzer, S. H. Payne, H. Pfnür, and M. Scheffler, *Phys. Rev. Lett.* **83**, 2993 (1999).

¹⁵P. Piercy, K. De'Bell, and H. Pfnür, *Phys. Rev. B* **45**, 1869

(1992).

¹⁶H. Tang, A. Van der Ven, and B. L. Trout, *Mol. Phys.* **102**, 273 (2004).

¹⁷A. R. Kortan and R. L. Park, *Phys. Rev. B* **23**, 6340 (1981).

¹⁸C. Schwennicke and H. Pfnür, *Phys. Rev. B* **56**, 10558 (1997).

¹⁹L. D. Roelofs, A. R. Kortan, T. L. Einstein, and R. L. Park, *J. Vac. Sci. Technol.* **18**, 492 (1981).

²⁰M. A. Mendez, W. Oed, A. Fricke, L. Hammer, K. Heinz, and K. Müller, *Surf. Sci.* **253**, 99 (1991).

²¹E. Schmidtke, C. Schwennicke, and H. Pfnür, *Surf. Sci.* **312**, 301 (1994).

²²L. D. Roelofs, A. R. Kortan, T. L. Einstein, and R. L. Park, *Phys. Rev. Lett.* **46**, 1465 (1981).

²³C. Schwenger, C. Voges, M. Sokolowski, and H. Pfnür, *Surf. Sci.* **307-309**, 781 (1994).

²⁴Z. Li, X. Liang, M. L. Stutzman, J. A. Spizuoco, S. Chandavarkar, and R. D. Diehl, *Surf. Sci.* **327**, 121 (1995).

²⁵C. Schwennicke, C. Voges, and H. Pfnür, *Surf. Sci.* **349**, 185 (1996).

²⁶P. H. Holloway and J. B. Hudson, *Surf. Sci.* **43**, 141 (1974).

²⁷A. Zunger, in *Statics and Dynamics of Alloy Phase Transformations*, edited by P. E. A. Turchy and A. Gonis (Plenum, New York, 1994), p. 361.

²⁸A. van de Walle and G. Ceder, *J. Phase Equilib.* **23**, 348 (2002).

²⁹M. H. F. Sluiter and Y. Kawazoe, *Phys. Rev. B* **68**, 085410 (2003).

- ³⁰A. Zunger, L. G. Wang, G. L. W. Hart, and M. Sanati, *Modell. Simul. Mater. Sci. Eng.* **10**, 685 (2002).
- ³¹C. Wolverton and A. Zunger, *Phys. Rev. Lett.* **75**, 3162 (1995).
- ³²M. Metropolis, A. W. Rosenbluth, M. N. Rosenbluth, A. H. Teller, and E. Teller, *J. Chem. Phys.* **21**, 1087 (1953).
- ³³F. Wang and D. P. Landau, *Phys. Rev. Lett.* **86**, 2050 (2001).
- ³⁴F. Wang and D. P. Landau, *Phys. Rev. E* **64**, 056101 (2001).
- ³⁵D. Chandler, *Introduction to Modern Statistical Mechanics* (Oxford University Press, New York, 1987).
- ³⁶Even though, formally, Ising-like lattice models are described as “fixed lattice” models; they have been shown to be able to describe the energetics and thermodynamics associated with large atomic displacements in alloys (Ref. 31). Thus, the effect of relaxation can be accounted for by using DFT energies of *fully relaxed* geometries to derive the lateral interaction parameters.
- ³⁷T. L. Einstein, *Langmuir* **7**, 2520 (1991).
- ³⁸T. L. Einstein, in *Handbook of Surface Science*, edited by W. N. Unertl (Elsevier, Amsterdam, 1996), Vol. I, p. 577.
- ³⁹J. M. Sanchez, F. Ducastelle, and D. Gratias, *Physica A* **128**, 334 (1984).
- ⁴⁰J. W. D. Connolly and A. R. Williams, *Phys. Rev. B* **27**, 5169 (1983).
- ⁴¹S. Müller, *J. Phys.: Condens. Matter* **15**, R1429 (2003).
- ⁴²P. Blaha, K. Schwarz, G. K. H. Madsen, D. Kvasnicka, and J. Luitz, *WIEN2K: An Augmented Plane Wave+Local Orbitals Program for Calculating Crystal Properties* (Techn. Universität Wien, Wien, Austria, 2001).
- ⁴³K. Schwarz, P. Blaha, and G. K. H. Madsen, *Comput. Phys. Commun.* **147**, 71 (2002).
- ⁴⁴J. P. Perdew, K. Burke, and M. Ernzerhof, *Phys. Rev. Lett.* **77**, 3865 (1996).
- ⁴⁵M. J. Gillan, *J. Phys.: Condens. Matter* **1**, 689 (1989).
- ⁴⁶R. Drautz, M. Fähnle, and J. M. Sanchez, *J. Phys.: Condens. Matter* **16**, 3843 (2004).
- ⁴⁷D. C. Montgomery and G. C. Runger, *Applied Statistics and Probability for Engineers*, 4th ed. (Wiley, New York, 2007).
- ⁴⁸The selection of candidate ECIs for the cluster expansion is based on the concept of maximal cluster. The maximal cluster and subclusters are defined by the principle of a complete set of cluster figures that is found within a circle of a given radius. For details see Refs. 28 and 29.
- ⁴⁹G. L. W. Hart, V. Blum, M. J. Walorski, and A. Zunger, *Nature Mater.* **4**, 391 (2005).
- ⁵⁰V. Blum, G. L. W. Hart, M. J. Walorski, and A. Zunger, *Phys. Rev. B* **72**, 165113 (2005).
- ⁵¹M. Borg, C. Stampfl, A. Mikkelsen, J. Gustafson, E. Lundgren, M. Scheffler, and J. Andersen, *ChemPhysChem* **6**, 1923 (2005).
- ⁵²R. Drautz and A. Díaz-Ortiz, *Phys. Rev. B* **73**, 224207 (2006).
- ⁵³S. G. Gilmour, *Statistician* **45**, 49 (1996).
- ⁵⁴D. P. Landau and K. Binder, *A Guide to Monte Carlo Simulations in Statistical Physics*, 2nd ed. (Cambridge University Press, Cambridge, England, 2005).
- ⁵⁵J. Glosli and M. Plischke, *Can. J. Phys.* **61**, 1515 (1983).
- ⁵⁶M. Schick, *Prog. Surf. Sci.* **11**, 245 (1981).
- ⁵⁷A. van de Walle and M. Asta, *Modell. Simul. Mater. Sci. Eng.* **10**, 521 (2002).
- ⁵⁸F. Mittendorfer, A. Eichler, and J. Hafner, *Surf. Sci.* **423**, 1 (1999).
- ⁵⁹H. B. Michaelson, *J. Appl. Phys.* **48**, 4729 (1977).
- ⁶⁰J. W. M. Frenken, R. G. Smeenk, and J. F. van der Veen, *Surf. Sci.* **135**, 147 (1983).
- ⁶¹H. C. Lu, E. P. Gusev, E. Garfunkel, and T. Gustafsson, *Surf. Sci.* **352-354**, 21 (1996).
- ⁶²C. Kittel, *Introduction to Solid State Physics*, 8th ed. (Wiley, New York, 2005).
- ⁶³A. Eichler, F. Mittendorfer, and J. Hafner, *Phys. Rev. B* **62**, 4744 (2000).
- ⁶⁴T. Li, B. Bhatia, and D. S. Sholl, *J. Chem. Phys.* **121**, 10241 (2004).
- ⁶⁵J. T. Stuckless, C. E. Wartnaby, S. J. B. D.-W. N. Al-Sarraf, and D. A. King, *J. Chem. Phys.* **106**, 2012 (1997).
- ⁶⁶U. von Barth, *Phys. Scr.* **T109**, 9 (2004).
- ⁶⁷P. Ugliengo and A. Damin, *Chem. Phys. Lett.* **366**, 683 (2002).
- ⁶⁸A. Michaelides and M. Scheffler, in *Textbook of Surface and Interface Science*, edited by K. Wandelt (Wiley-VCH, Berlin, 2008), Vol. I.
- ⁶⁹J. Kohanoff, *Electronic Structure Calculations for Solid and Molecules*, 1st ed. (Cambridge University Press, London, 2006).
- ⁷⁰M. Pedio, L. Becker, B. Hillert, S. D’Addato, and J. Haase, *Phys. Rev. B* **41**, 7462 (1990).
- ⁷¹A. Kiejna, G. Kresse, J. Rogal, A. De Sarkar, K. Reuter, and M. Scheffler, *Phys. Rev. B* **73**, 035404 (2006).
- ⁷²A. E. Mattsson, P. A. Schultz, M. P. Desjarlais, T. R. Mattsson, and K. Leung, *Modell. Simul. Mater. Sci. Eng.* **13**, R1 (2005).
- ⁷³D. T. Vu Grimsby, Y. K. Wu, and K. A. R. Mitchell, *Surf. Sci.* **232**, 51 (1990).
- ⁷⁴M. B. Knickelbein, *J. Chem. Phys.* **116**, 9703 (2002).
- ⁷⁵S. Yamagishi, S. J. Jenkins, and D. A. King, *Surf. Sci.* **543**, 12 (2003).
- ⁷⁶R. J. Birgeneau, J. Cordes, G. Dolling, and A. D. B. Woods, *Phys. Rev.* **136**, A1359 (1964).
- ⁷⁷G. Tisdale and S. J. Sibener, *Surf. Sci.* **311**, 360 (1994).
- ⁷⁸Y. Zhang, V. Blum, and K. Reuter, *Phys. Rev. B* **75**, 235406 (2007).
- ⁷⁹A confidence interval is an estimated range of values with a specified probability of containing the true population value of a parameter (see, e.g., Ref. 47).
- ⁸⁰By excluding the configurations in the biggest cell used in this study, i.e., the (3×4) unit cell, we have tested that the critical temperature for $\Theta=1/4$ ML, for a parameter set equivalent to set I, lies in the 100 K interval of Fig. 7. Likewise, including eight to ten more hcp configurations leads to critical temperatures inside of this interval. These results suggest that using bigger units cells and including more hcp configurations would not lead to appreciably different critical temperatures.
- ⁸¹L. D. Roelofs, in *Chemistry and Physics of Solid Surfaces*, edited by R. Vanselow and R. Howe (Springer, Berlin, 1982), Vol. IV, p. 219.
- ⁸²M. O. M. Fukugita, H. Mino, and A. Ukawa, *J. Phys. A* **23**, L561 (1990).
- ⁸³C. Voges and H. Pfnür, *Phys. Rev. B* **57**, 3345 (1998).
- ⁸⁴N. C. Bartelt, T. L. Einstein, and L. D. Roelofs, *Phys. Rev. B* **32**, 2993 (1985).
- ⁸⁵T. J. Stasevich, T. L. Einstein, and S. Stolbov, *Phys. Rev. B* **73**, 115426 (2006).
- ⁸⁶Y. Tiwary and K. A. Fichthorn, *Phys. Rev. B* **75**, 235451 (2007).
- ⁸⁷C. Stampfl and M. Scheffler, *Phys. Rev. B* **54**, 2868 (1996).